

On the State Space Geometry of the Kuramoto–Sivashinsky Flow in a Periodic Domain*

Predrag Cvitanović[†], Ruslan L. Davidchack[‡], and Evangelos Siminos[†]

Abstract. The continuous and discrete symmetries of the Kuramoto–Sivashinsky system restricted to a spatially periodic domain play a prominent role in shaping the invariant sets of its chaotic dynamics. The continuous spatial translation symmetry leads to relative equilibrium (traveling wave) and relative periodic orbit (modulated traveling wave) solutions. The discrete symmetries lead to existence of equilibrium and periodic orbit solutions, induce decomposition of state space into invariant subspaces, and enforce certain structurally stable heteroclinic connections between equilibria. We show, for the example of a particular small-cell Kuramoto–Sivashinsky system, how the geometry of its dynamical state space is organized by a rigid “cage” built by heteroclinic connections between equilibria, and demonstrate the preponderance of unstable relative periodic orbits and their likely role as the skeleton underpinning spatiotemporal turbulence in systems with continuous symmetries. We also offer novel visualizations of the high-dimensional Kuramoto–Sivashinsky state space flow through projections onto low-dimensional, PDE representation-independent, dynamically invariant intrinsic coordinate frames, as well as in terms of the physical, symmetry invariant energy transfer rates.

Key words. relative periodic orbits, chaos, turbulence, continuous symmetry, Kuramoto–Sivashinsky equation

AMS subject classifications. 35B05, 35B10, 37L05, 37L20, 76F20, 65H10, 90C53

DOI. 10.1137/070705623

1. Introduction. Recent experimental and theoretical advances [24] support a dynamical vision of turbulence: For any finite spatial resolution, a turbulent flow follows approximately for a finite time a pattern belonging to a finite alphabet of admissible patterns. The long-term dynamics is a walk through the space of these unstable patterns. The question is how to characterize and classify such patterns. Here we follow the seminal Hopf paper [26] and visualize turbulence not as a sequence of spatial snapshots in turbulent evolution, but as a trajectory in an infinite-dimensional state space in which an instant in turbulent evolution is a unique point. In the dynamical systems approach, theory of turbulence for a given system, with given boundary conditions, is given by (a) the geometry of the state space and (b) the associated natural measure, that is, the likelihood that asymptotic dynamics visits a given state space region.

We pursue this program in context of the Kuramoto–Sivashinsky (KS) equation, one of the simplest physically interesting spatially extended nonlinear systems. Holmes, Lumley,

*Received by the editors October 17, 2007; accepted for publication (in revised form) by D. Barkley October 14, 2009; published electronically DATE.

<http://www.siam.org/journals/siads/x-x/70562.html>

[†]School of Physics, Georgia Institute of Technology, Atlanta, GA 30332-0430 (cvitanovic@physics.gatech.edu, siminos@gatech.edu). The third author was partly supported by NSF grant DMS-0807574.

[‡]Department of Mathematics, University of Leicester, University Road, Leicester LE1 7RH, UK (rld8@mcs.le.ac.uk). This author was partly supported by EPSRC under grant GR/S98986/01.

and Berkooz [25] offer a delightful discussion of why this system deserves study as a staging ground for studying turbulence in full-fledged Navier–Stokes boundary shear flows.

Flows described by partial differential equations (PDEs) are said to be infinite-dimensional because if one writes them down as a set of ordinary differential equations (ODEs), a set of infinitely many ODEs is needed to represent the dynamics of one PDE. Even though their state space is thus infinite-dimensional, the long-time dynamics of viscous flows, such as Navier–Stokes, and PDEs modeling them, such as Kuramoto–Sivashinsky equations, exhibits, when dissipation is high and the system spatial extent small, apparent “low-dimensional” dynamical behaviors. For some of these the asymptotic dynamics is known to be confined to a finite-dimensional *inertial manifold*, though the rigorous upper bounds on this dimension are not of much use in practice.

For large spatial extent the complexity of the spatial motions also needs to be taken into account. The systems whose spatial correlations decay sufficiently fast, and for which the attractor dimension and number of positive Lyapunov exponents diverges with system size, are said [27, 41, 9] to be extensive, “spatio-temporally chaotic,” or “weakly turbulent.” Conversely, for small system sizes the accurate description might require a large set [19] of coupled ODEs, but dynamics can still be low-dimensional in the sense that it is characterized with one or a few positive Lyapunov exponents. There is no wide range of scales involved, nor decay of spatial correlations, and the system is in this sense only “chaotic.”

For a subset of physicists and mathematicians who study idealized “fully developed,” “homogenous” turbulence the generally accepted usage is that the “turbulent” fluid is characterized by a range of scales and an energy cascade describable by statistical assumptions [15]. What experimentalists, engineers, geophysicists, and astrophysicists actually observe looks nothing like a “fully developed turbulence.” In the physically driven wall-bounded shear flows, the turbulence is dominated by unstable *coherent structures*, that is, localized recurrent vortices, rolls, streaks, and the like. The statistical assumptions fail, and a dynamical systems description from first principles is called for [25].

The set of invariant solutions investigated here is embedded into a finite-dimensional inertial manifold [13] in a nontrivial, nonlinear way. “Geometry” in the title of this paper refers to our attempt to systematically triangulate this set in terms of dynamically invariant solutions (equilibria, periodic orbits, ...) and their unstable manifolds, in a PDE representation and numerical simulation algorithm-independent way. The goal is to describe a given turbulent flow quantitatively, not model it qualitatively by a low-dimensional model. For the case investigated here, the state space representation dimension $d \sim 10^2$ is set by requiring that the exact invariant solutions that we compute be accurate to $\sim 10^{-5}$.

Here comes our quandary. If we ban the words turbulence and spatiotemporal chaos from our study of small extent systems, the relevance of what we do to larger systems is obscured. The exact unstable coherent structures that we determine pertain not only to the spatially small chaotic systems, but also the spatially large spatiotemporally chaotic and the spatially very large turbulent systems. So, for the lack of more precise nomenclature, we take the liberty of using the terms chaos, spatiotemporal chaos, and turbulence interchangeably.

In previous work, the state space geometry and the natural measure for this system have been studied [6, 37, 38] in terms of unstable periodic solutions restricted to the antisymmetric subspace of the KS dynamics.

The focus in this paper is on the role that continuous symmetries play in spatiotemporal dynamics. The notion of exact periodicity in time is replaced by the notion of relative spatio-temporal periodicity, and relative equilibria and relative periodic orbits here play the role that the equilibria and periodic orbits played in the earlier studies. Our search for relative periodic orbits in the KS system was inspired by the investigation of López et al. [40] into relative periodic orbits of the complex Ginzburg–Landau equation. However, there is a vast literature on relative periodic orbits since their first appearance, in Poincaré study of the three-body problem [5, 47], where the Lagrange points are the relative equilibria. Such orbits arise in dynamics of systems with continuous symmetries, such as motions of rigid bodies, gravitational N -body problems, molecules, and nonlinear waves. Recently Viswanath [48] has found both relative equilibria and relative periodic orbits in the plane Couette problem. A Hopf bifurcation of a traveling wave [1, 2, 34] induces a small time-dependent modulation. Brown and Kevrekidis [4] study bifurcation branches of periodic orbits and relative periodic orbits in the KS system in great detail. For our system size ($\alpha = 49.04$ in their notation) they identify a periodic orbit branch. In this context relative periodic orbits are referred to as “modulated traveling waves.” For fully chaotic flows we find this notion too narrow. We compute 60,000 periodic orbits and relative periodic orbits that are in no sense small “modulations” of other solutions; hence our preference for the well established notion of a “relative periodic orbit.”

Building upon the pioneering work of [32, 22, 4], we undertake here a study of the KS dynamics for a specific system size, $L = 22$, sufficiently large to exhibit many of the features typical of turbulent dynamics observed in large KS systems but small enough to lend itself to a detailed exploration of the equilibria and relative equilibria, their stable/unstable manifolds, determination of a large number of relative periodic orbits, and a preliminary exploration of the relation between the observed spatiotemporal turbulent patterns and the relative periodic orbits.

In presence of a continuous symmetry, any solution belongs to a group orbit of equivalent solutions. The problem: If one is to generalize the periodic orbit theory to this setting, one needs to understand what is meant by solutions being nearby (shadowing) when each solution belongs to a manifold of equivalent solutions. In a forthcoming publication [45] we resolve this puzzle by implementing symmetry reduction. Here we demonstrate that, for relative periodic orbits visiting the neighborhood of equilibria, if one picks any particular solution, the universe of all other solutions is rigidly fixed through a web of heteroclinic connections between them. This insight garnered from study of a 1-dimensional KS PDEs is more remarkable still when applied to the plane Couette flow [19], with 3-dimensional velocity fields and two translational symmetries.

The main results presented here are the following: (a) Dynamics visualized through physical, symmetry-invariant observables, such as “energy,” dissipation rate, etc., and through projections onto dynamically invariant, PDE-discretization-independent state space coordinate frames (section 3). (b) Existence of a rigid “cage” built by heteroclinic connections between equilibria (section 4). (c) Preponderance of unstable relative periodic orbits and their likely role as the skeleton underpinning spatiotemporal turbulence in systems with continuous symmetries (section 6).

2. Kuramoto–Sivashinsky equation. The KS system [36, 46], which arises in the description of stability of flame fronts, reaction-diffusion systems, and many other physical

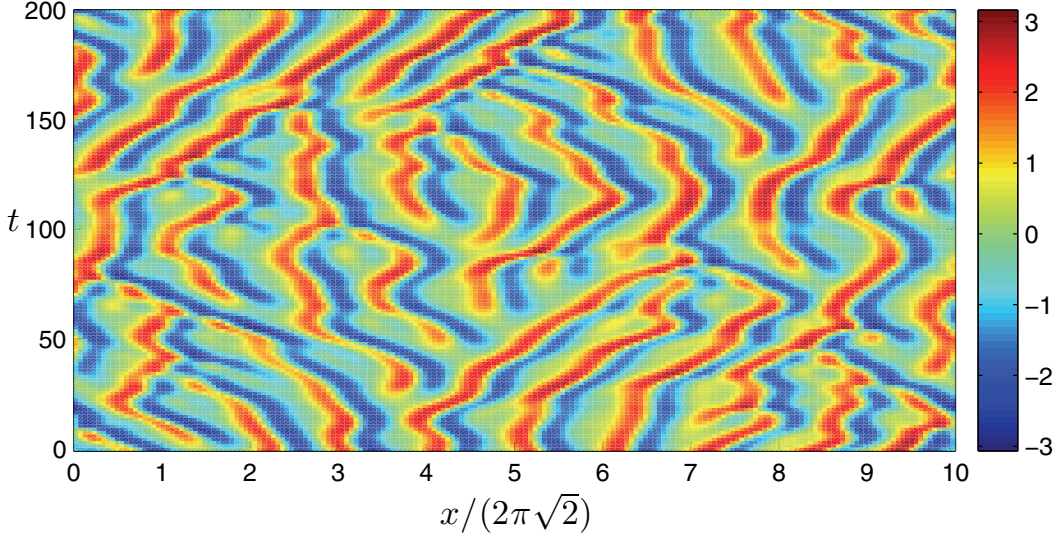


Figure 1. A typical spatiotemporally chaotic solution of the KS equation, system size $L = 20\pi\sqrt{2} \approx 88.86$. The x coordinate is scaled with the most unstable wavelength $2\pi\sqrt{2}$, which is approximately also the mean wavelength of the turbulent flow. The color bar indicates the color scheme for $u(x, t)$, used also for the subsequent figures of this type.

settings [32], is one of the simplest nonlinear PDEs that exhibit spatiotemporally chaotic behavior. In the formulation adopted here, the time evolution of the *flame front velocity* $u = u(x, t)$ on a periodic domain $u(x, t) = u(x + L, t)$ is given by

$$(2.1) \quad u_t = F(u) = -\frac{1}{2}(u^2)_x - u_{xx} - u_{xxx}, \quad x \in \left[-\frac{L}{2}, \frac{L}{2}\right].$$

Here $t \geq 0$ is the time, and x is the spatial coordinate. The subscripts x and t denote partial derivatives with respect to x and t . In what follows we shall state results of all calculations either in units of the “dimensionless system size” \tilde{L} , or the system size $L = 2\pi\tilde{L}$. Figure 1 presents a typical turbulent evolution for KS. All numerical results presented in this paper are for the system size $\tilde{L} = 22/2\pi = 3.5014\dots$, for which a structurally stable chaotic attractor is observed (see Figure 4). Spatial periodicity $u(x, t) = u(x + L, t)$ makes it convenient to work in the Fourier space,

$$(2.2) \quad u(x, t) = \sum_{k=-\infty}^{+\infty} a_k(t) e^{ikx/\tilde{L}},$$

with the 1-dimensional PDE (2.1) replaced by an infinite set of ODEs for the complex Fourier coefficients $a_k(t)$:

$$(2.3) \quad \dot{a}_k = v_k(a) = (q_k^2 - q_k^4) a_k - i \frac{q_k}{2} \sum_{m=-\infty}^{+\infty} a_m a_{k-m},$$

where $q_k = k/\tilde{L}$. Since $u(x, t)$ is real, $a_k = a_{-k}^*$, and we can replace the sum by an $m > 0$ sum.

Due to the hyperviscous damping u_{xxxx} , long-time solutions of the KS equation are smooth, a_k drop off fast with k , and truncations of (2.3) to $16 \leq N \leq 128$ terms yield accurate solutions for system sizes considered here (see Appendix A). Robustness of the long-time dynamics of the KS system as a function of the number of Fourier modes kept in truncations of (2.3) is, however, a subtle issue. Adding an extra mode to a truncation of the system introduces a small perturbation in the space of dynamical systems. However, due to the lack of structural stability as a function of both the truncation N and the system size L , a small variation in a system parameter can (and often will) throw the dynamics into a different asymptotic state. For example, an asymptotic attractor which appears to be chaotic in an N -dimensional state space truncation can collapse into an attractive cycle for $(N + 1)$ dimensions. Therefore, the selection of parameter L for which a structurally stable chaotic dynamics exists and can be studied is rather subtle. We have found that the value of $L = 22$ studied in section 4 satisfies these requirements. In particular, all of the equilibria and relative equilibria persist and remain unstable when N is increased from 32 (the value we use in our numerical investigations) to 64 and 128. Nearly all of the relative periodic orbits we have found for this system also exist and remain unstable for larger values of N as well as for smaller values of the integration step size (see Appendix C for details).

2.1. Symmetries of the KS equation. The KS equation is Galilean invariant: If $u(x, t)$ is a solution, then $u(x - ct, t) - c$, with c an arbitrary constant speed, is also a solution. Without loss of generality, in our calculations we shall set the mean velocity of the front to zero,

$$(2.4) \quad \int dx u = 0.$$

As $\dot{a}_0 = 0$ in (2.3), a_0 is a conserved quantity fixed to $a_0 = 0$ by the condition (2.4). G , the group of actions $g \in G$ on a state space (reflections, translations, etc.), is a symmetry of the KS flow (2.1) if $g u_t = F(g u)$. The KS equation is time translationally invariant and space translationally invariant on a periodic domain under the 1-parameter group of $O(2) : \{\tau_{\ell/L}, R\}$. If $u(x, t)$ is a solution, then $\tau_{\ell/L} u(x, t) = u(x + \ell, t)$ is an equivalent solution for any shift $-L/2 < \ell \leq L/2$, as is the reflection (“parity” or “inversion”)

$$(2.5) \quad R u(x) = -u(-x).$$

The translation operator action on the Fourier coefficients (2.2), represented here by a complex-valued vector $a = \{a_k \in \mathbb{C} \mid k = 1, 2, \dots\}$, is given by

$$(2.6) \quad \tau_{\ell/L} a = \mathbf{g}(\ell) a,$$

where $\mathbf{g}(\ell) = \text{diag}(e^{iq_k \ell})$ is a complex-valued diagonal matrix, which amounts to the k th mode complex plane rotation by an angle $k \ell / \tilde{L}$. The reflection acts on the Fourier coefficients by complex conjugation,

$$(2.7) \quad R a = -a^*.$$

Reflection generates the dihedral subgroup $D_1 = \{1, R\}$ of $O(2)$. Let \mathbb{U} be the space of real-valued velocity fields periodic and square integrable on the interval $\Omega = [-L/2, L/2]$,

$$(2.8) \quad \mathbb{U} = \{u \in L^2(\Omega) \mid u(x) = u(x+L)\}.$$

A continuous symmetry maps each state $u \in \mathbb{U}$ to a manifold of functions with identical dynamic behavior. Relation $R^2 = 1$ induces linear decomposition $u(x) = u^+(x) + u^-(x)$, $u^\pm(x) = P^\pm u(x) \in \mathbb{U}^\pm$, into irreducible subspaces $\mathbb{U} = \mathbb{U}^+ \oplus \mathbb{U}^-$, where

$$(2.9) \quad P^+ = \frac{(1+R)}{2}, \quad P^- = \frac{(1-R)}{2},$$

are the antisymmetric/symmetric projection operators. Applying P^+ , P^- on the KS equation (2.1), we have [32]

$$(2.10) \quad \begin{aligned} u_t^+ &= -(u^+ u_x^+ + u^- u_x^-) - u_{xx}^+ - u_{xxxx}^+, \\ u_t^- &= -(u^+ u_x^- + u^- u_x^+) - u_{xx}^- - u_{xxxx}^-. \end{aligned}$$

If $u^- = 0$, KS flow is confined to the antisymmetric \mathbb{U}^+ subspace,

$$(2.11) \quad u_t^+ = -u^+ u_x^+ - u_{xx}^+ - u_{xxxx}^+,$$

but otherwise the nonlinear terms in (2.10) mix the two subspaces.

Any rational shift $\tau_{1/m} u(x) = u(x+L/m)$ generates a discrete cyclic subgroup C_m of $O(2)$, also a symmetry of KS system. Reflection together with C_m generates another symmetry of the KS system, the dihedral subgroup D_m of $O(2)$. The only nonzero Fourier components of a solution invariant under C_m are $a_{jm} \neq 0$, $j = 1, 2, \dots$, while for a solution invariant under D_m we also have the condition $\text{Re } a_j = 0$ for all j . D_m reduces the dimensionality of state space and aids computation of equilibria and periodic orbits within it. For example, the 1/2-cell translations

$$(2.12) \quad \tau_{1/2} u(x) = u\left(x + \frac{L}{2}\right)$$

and reflections generate $O(2)$ subgroup $D_2 = \{1, R, \tau, \tau R\}$, which reduces the state space into four irreducible subspaces (for brevity, here $\tau = \tau_{1/2}$):

$$(2.13) \quad \begin{array}{ccccc} & & \tau & R & \tau R \\ P^{(1)} &= \frac{1}{4}(1 + \tau + R + \tau R) & S & S & S \\ P^{(2)} &= \frac{1}{4}(1 + \tau - R - \tau R) & S & A & A \\ P^{(3)} &= \frac{1}{4}(1 - \tau + R - \tau R) & A & S & A \\ P^{(4)} &= \frac{1}{4}(1 - \tau - R + \tau R) & A & A & S. \end{array}$$

$P^{(j)}$ is the projection operator onto $u^{(j)}$ irreducible subspace, and the last three columns refer to the symmetry (or antisymmetry) of $u^{(j)}$ functions under reflection and 1/2-cell shift. By the same argument that identified (2.11) as the invariant subspace of KS, here the KS flow stays within the $\mathbb{U}^S = \mathbb{U}^{(1)} + \mathbb{U}^{(2)}$ irreducible D_1 subspace of u profiles symmetric under 1/2-cell shifts.

While in general the bilinear term $(u^2)_x$ mixes the irreducible subspaces of D_n , for D_2 there are four subspaces invariant under the flow [32]:

- $\{0\}$: the $u(x) = 0$ equilibrium,
- $\mathbb{U}^+ = \mathbb{U}^{(1)} + \mathbb{U}^{(3)}$: the reflection D_1 irreducible space of antisymmetric $u(x)$,
- $\mathbb{U}^S = \mathbb{U}^{(1)} + \mathbb{U}^{(2)}$: the shift D_1 irreducible space of $L/2$ shift symmetric $u(x)$,
- $\mathbb{U}^{(1)}$: the D_2 irreducible space of $u(x)$ invariant under $x \mapsto L/2 - x$, $u \mapsto -u$.

With the continuous translational symmetry eliminated within each subspace, there are no relative equilibria and relative periodic orbits, and one can focus on the equilibria and periodic orbits only, as was done for \mathbb{U}^+ in [6, 37, 38]. In the Fourier representation, the $u \in \mathbb{U}^+$ antisymmetry amounts to having purely imaginary coefficients, since $a_{-k} = a_k^* = -a_k$. The 1/2 cell-size shift $\tau_{1/2}$ generated 2-element discrete subgroup $\{1, \tau_{1/2}\}$ is of particular interest, because in the \mathbb{U}^+ subspace the translational invariance of the full system reduces to invariance under discrete translation (2.12) by half a spatial period $L/2$.

Each of the above dynamically invariant subspaces is unstable under small perturbations, and generic solutions of the KS equation belong to the full space. Nevertheless, since all equilibria of the KS flow studied in this paper lie in the \mathbb{U}^+ subspace (see section 4), \mathbb{U}^+ plays an important role for the global geometry of the flow. The linear stability matrices of these equilibria have eigenvectors both in and outside of \mathbb{U}^+ and need to be computed in the full state space.

2.2. Equilibria and relative equilibria. Equilibria (or the steady solutions) are the fixed profile time invariant solutions,

$$(2.14) \quad u(x, t) = u_q(x).$$

Due to the translational symmetry, the KS system also allows for relative equilibria (traveling waves, rotating waves), characterized by a fixed profile $u_q(x)$ moving with constant speed c , that is,

$$(2.15) \quad u(x, t) = u_q(x - ct).$$

Here suffix $_q$ labels a particular invariant solution. Because of the reflection symmetry (2.5), the relative equilibria come in counter-traveling pairs $u_q(x - ct)$, $-u_q(-x + ct)$.

The relative equilibrium condition for the KS PDE (2.1) is the ODE

$$(2.16) \quad \frac{1}{2}(u^2)_x + u_{xx} + u_{xxx} = c u_x,$$

which can be analyzed as a dynamical system in its own right. Integrating once, we get

$$(2.17) \quad \frac{1}{2}u^2 - cu + u_x + u_{xxx} = E.$$

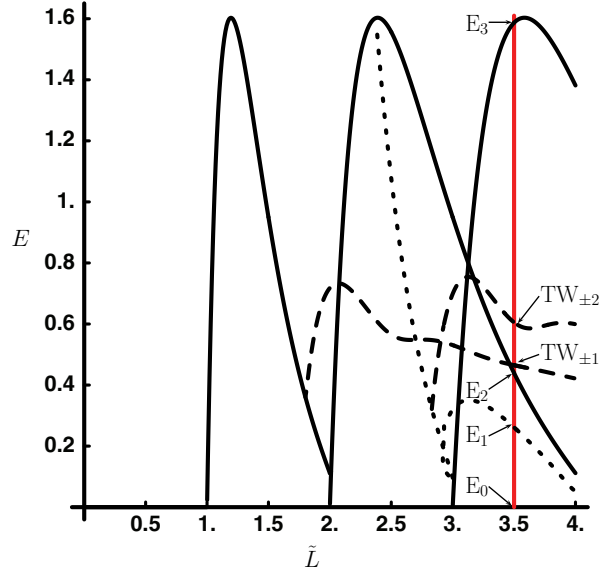


Figure 2. The energy (3.6) of the equilibria and relative equilibria that exist up to $L = 22$, $\tilde{L} = 3.5014\dots$, plotted as a function of the system size $\tilde{L} = L/2\pi$ (additional equilibria, not present at $L = 22$, are given in [22]). Solid curves denote n -cell solutions E_2 and E_3 , dotted curves the GLMRT equilibrium E_1 , and dashed curves the relative equilibria $TW_{\pm 1}$ and $TW_{\pm 2}$. The parameter α of [32, 22] is related to the system size by $\tilde{L} = \sqrt{\alpha/4}$.

This equation can be interpreted as a three-dimensional dynamical system with spatial coordinate x playing the role of “time,” and the integration constant E can be interpreted as “energy”; see section 3.

For $E > 0$ there is rich E -dependent dynamics, with fractal sets of bounded solutions investigated in depth by Michelson [42]. For $\tilde{L} < 1$ the only equilibrium of the system is the globally attracting constant solution $u(x, t) = 0$, denoted E_0 from now on. With increasing system size L the system undergoes a series of bifurcations. The resulting equilibria and relative equilibria are described in the classical papers of Kevrekidis, Nicolaenko, and Scovel [32], and Greene and Kim [22], among others. The relevant bifurcations up to the system size investigated here are summarized in Figure 2: At $\tilde{L} = 22/2\pi = 3.5014\dots$, the equilibria are the constant solution E_0 ; the equilibrium E_1 , called GLMRT by Greene and Kim [39, 22]; the 2- and 3-cell states E_2 and E_3 ; and the pairs of relative equilibria $TW_{\pm 1}$, $TW_{\pm 2}$. All equilibria are in the antisymmetric subspace \mathcal{U}^+ , while E_2 is also invariant under D_2 , and E_3 under D_3 .

In the Fourier representation the time dependence of the relative equilibria is

$$(2.18) \quad a_k(t)e^{-itcq_k} = a_k(0).$$

Differentiating with respect to time, we obtain the Fourier space version of the relative equilibrium condition (2.16),

$$(2.19) \quad v_k(a) - iq_k c a_k = 0,$$

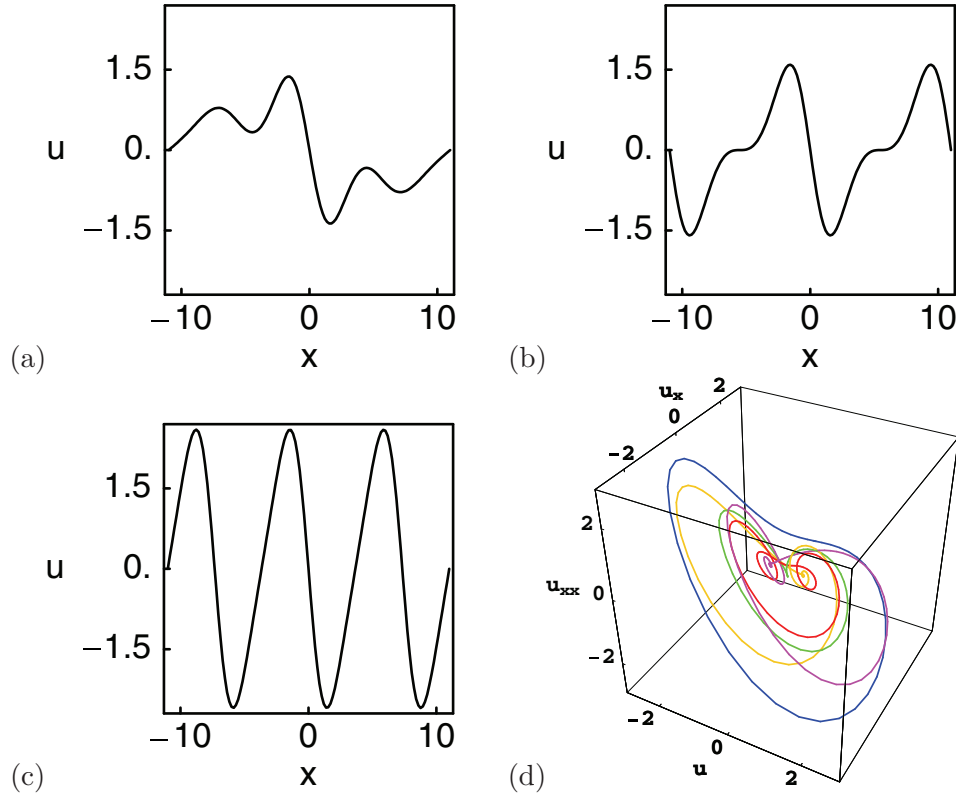


Figure 3. (a) E_1 , (b) E_2 , and (c) E_3 equilibria. The E_0 equilibrium is the $u(x) = 0$ solution. (d) (u, u_x, u_{xx}) representation of (red) E_1 , (green) E_2 , (blue) E_3 equilibria, (purple) TW_{+1} , and (orange) TW_{-1} relative equilibria. $L = 22$ system size.

which we solve for (time-independent) a_k and c . Periods of spatially periodic equilibria are L/n with integer n . Every time the system size crosses $\tilde{L} = n$, n -cell states are generated through pitchfork bifurcations off the $u = 0$ equilibrium. Due to the translational invariance of the KS equation, they form invariant circles in the full state space. In the \mathbb{U}^+ subspace considered here, they correspond to $2n$ points, each shifted by $L/2n$. For a sufficiently small L the number of equilibria is small and concentrated on the low wavenumber end of the Fourier spectrum.

In a periodic box of size L both equilibria and relative equilibria are periodic solutions embedded in 3-dimensional space, conveniently represented as loops in (u, u_x, u_{xx}) space; see Figure 3(d). In this representation the continuous translation symmetry is automatic—a rotation in the $[0, L]$ periodic domain moves only the points along the loop. For an equilibrium the points are stationary in time; for relative equilibrium they move in time, but in either case, the loop remains invariant. So we do not have the problem that we encounter in the Fourier representation, where, seen from the frame of one of the equilibria, the rest trace out circles under the action of continuous symmetry translations.

From (2.3) we see that the origin $u(x, t) = 0$ has Fourier modes as the linear stability eigenvectors (see Appendix B). The $|k| < \tilde{L}$ long wavelength perturbations of the flat-front

equilibrium are linearly unstable, while for $|k|$ sufficiently larger than \tilde{L} the short wavelength perturbations are strongly contractive. The high k eigenvalues, corresponding to rapid variations of the flame front, decay so fast that the corresponding eigendirections are physically irrelevant. Indeed, [49] shows that the chaotic solutions of spatially extended dissipative systems evolve within an inertial manifold spanned by a finite number of physical modes, hyperbolically isolated from a set of residual degrees of freedom with high k , themselves individually isolated from each other. The most unstable mode, nearest to $|k| = \tilde{L}/\sqrt{2}$, sets the scale of the mean wavelength $\sqrt{2}$ of the KS turbulent dynamics; see Figure 1.

2.3. Relative periodic orbits, symmetries, and periodic orbits. The KS equation (2.1) is time translationally invariant, and space translationally invariant under the 1-dimensional Lie group of $O(2)$ rotations: If $u(x, t)$ is a solution, then $u(x + \ell, t)$ and $-u(-x, t)$ are equivalent solutions for any $-L/2 < \ell \leq L/2$. As a result of invariance under $\tau_{\ell/L}$, the KS equation can have relative periodic orbit solutions with a profile $u_p(x)$, period T_p , and a nonzero shift ℓ_p ,

$$(2.20) \quad \tau_{\ell_p/L} u(x, T_p) = u(x + \ell_p, T_p) = u(x, 0) = u_p(x).$$

Relative periodic orbits (2.20) are periodic in the $c_p = \ell_p/T_p$ corotating frame (see Figure 16), but in the stationary frame their trajectories are quasi-periodic. Due to the reflection symmetry (2.5) of the KS equation, every relative periodic orbit $u_p(x)$ with shift ℓ_p has a symmetric partner $-u_p(-x)$ with shift $-\ell_p$.

Due to invariance under reflections, the KS equation can also have relative periodic orbits *with reflection*, which are characterized by a profile $u_p(x)$ and period T_p ,

$$(2.21) \quad Ru(x + \ell, T_p) = -u(-x - \ell, T_p) = u(x + \ell, 0) = u_p(x),$$

giving the family of equivalent solutions parameterized by ℓ (as the choice of the reflection point is arbitrary, the shift can take any value in $-L/2 < \ell \leq L/2$).

Armbruster, Guckenheimer, and Holmes [2, 1] and Brown and Kevrekidis [4] (see also [34]) link the birth of relative periodic orbits to an infinite period global bifurcation involving a heteroclinic loop connecting equilibria or a bifurcation of relative equilibria, and also report creation of relative periodic orbit branches through bifurcation of periodic orbits.

As ℓ is continuous in the interval $[-L/2, L/2]$, the likelihood of a relative periodic orbit with $\ell_p = 0$ shift is zero, unless an exact periodicity is enforced by a discrete symmetry, such as the dihedral symmetries discussed above. If the shift ℓ_p of a relative periodic orbit with period T_p is such that ℓ_p/L is a rational number, then the orbit is periodic with period nT_p . The likelihood of finding such periodic orbits is also zero.

However, due to the KS equation invariance under the dihedral D_n and cyclic C_n subgroups, the following types of periodic orbits are possible:

(a) The periodic orbit lies within a subspace pointwise invariant under the action of D_n or C_n . For instance, for D_1 this is the \mathbb{U}^+ antisymmetric subspace, $-u_p(-x) = u_p(x)$, and $u(x, T_p) = u(x, 0) = u_p(x)$. The periodic orbits found in [6, 38] are all in \mathbb{U}^+ , as the dynamics is restricted to antisymmetric subspace. For $L = 22$ the dynamics in \mathbb{U}^+ is dominated by attracting (within the subspace) heteroclinic connections, and thus we have no periodic orbits of this type, or in any other of the D_n -invariant subspaces; see section 4.

(b) The periodic orbit satisfies

$$(2.22) \quad u(x, t + T_p) = \gamma u(x, t)$$

for some group element $\gamma \in O(2)$ such that $\gamma^m = e$ for some integer m so that the orbit repeats after time mT_p (see [21] for a general discussion of conditions on the symmetry of a periodic orbit). If an orbit is of reflection type (2.21), $R\tau_{\ell/L}u(x, T_p) = -u(-x - \ell, T_p) = u(x, 0)$, then it is preperiodic to a periodic orbit with period $2T_p$. Indeed, since $(R\tau_{\ell/L})^2 = R^2 = 1$ and the KS solutions are time translation invariant, it follows from (2.21) that

$$u(x, 2T_p) = R\tau_{\ell/L}u(x, T_p) = (R\tau_{\ell/L})^2u(x, 0) = u(x, 0).$$

Thus any shift acquired during time 0 to T_p is compensated by the opposite shift during evolution from T_p to $2T_p$. All periodic orbits we have found for $L = 22$ are of type (2.22) with $\gamma = R$. Preperiodic orbits with $\gamma \in C_n$ have been found by Brown and Kevrekidis [4] for KS system sizes larger than ours, but we have not found any for $L = 22$. Preperiodic orbits are a hallmark of any dynamical system with a discrete symmetry, where they have a natural interpretation as periodic orbits in the fundamental domain [12, 11].

3. Energy transfer rates. In physical settings where the observation times are much longer than the dynamical turnover and Lyapunov times (statistical mechanics, quantum physics, turbulence), periodic orbit theory [11] provides highly accurate predictions of measurable long-time averages such as the dissipation and the turbulent drag [19]. Physical predictions have to be independent of a particular choice of ODE representation of the PDE under consideration and, most importantly, invariant under all symmetries of the dynamics. In this section we discuss a set of such physical observables for the 1-dimensional KS invariant under reflections and translations. They offer a representation of dynamics in which the symmetries are explicitly quotiented out. We shall use these observables in section 8 to visualize a set of solutions on these coordinates.

The space average of a function $a = a(x, t) = a(u(x, t))$ on the interval L ,

$$(3.1) \quad \langle a \rangle = \frac{1}{L} \oint dx a(x, t),$$

is in general time-dependent. Its mean value is given by the time average

$$(3.2) \quad \bar{a} = \lim_{t \rightarrow \infty} \frac{1}{t} \int_0^t d\tau \langle a \rangle = \lim_{t \rightarrow \infty} \frac{1}{t} \int_0^t \frac{1}{L} \oint d\tau dx a(x, \tau).$$

The mean value of $a = a(u_q) \equiv a_q$ evaluated on equilibrium or relative equilibrium $u(x, t) = u_q(x - ct)$, labeled by q as in (2.15), is

$$(3.3) \quad \bar{a}_q = \langle a \rangle_q = a_q.$$

Evaluation of the infinite time average (3.2) on a function of a periodic orbit or relative periodic orbit $u_p(x, t) = u_p(x + \ell_p, t + T_p)$ requires only a single T_p traversal,

$$(3.4) \quad \bar{a}_p = \frac{1}{T_p} \int_0^{T_p} d\tau \langle a \rangle.$$

Equation (2.1) can be written as

$$(3.5) \quad u_t = -V_x, \quad V(x, t) = \frac{1}{2}u^2 + u_x + u_{xxx}.$$

If u is “flame-front velocity,” then E , defined in (2.17), can be interpreted as the mean energy density. So, even though KS is a phenomenological small-amplitude equation, the time-dependent L^2 norm of u ,

$$(3.6) \quad E = \frac{1}{L} \oint dx V(x, t) = \frac{1}{L} \oint dx \frac{u^2}{2},$$

has a physical interpretation [22] as the average “energy” density of the flame front. This analogy to the mean kinetic energy density for the Navier–Stokes equation motivates what follows.

The energy (3.6) is intrinsic to the flow and independent of the particular ODE basis set chosen to represent the PDE. However, as the Fourier amplitudes are eigenvectors of the translation operator, in the Fourier space the energy is a diagonalized quadratic norm,

$$(3.7) \quad E = \sum_{k=-\infty}^{\infty} E_k, \quad E_k = \frac{1}{2}|a_k|^2,$$

and explicitly invariant term-by-term under translations (2.6) and reflections (2.5).

Take time derivative of the energy density (3.6), substitute (2.1), and integrate by parts. Total derivatives vanish by the spatial periodicity on the L domain:

$$(3.8) \quad \begin{aligned} \dot{E} &= \langle u_t u \rangle = - \left\langle \left(\frac{u^2}{2} + u_x + u_{xxx} \right)_x u \right\rangle \\ &= \left\langle \frac{u_x u^2}{2} + u_x^2 + u_x u_{xxx} \right\rangle. \end{aligned}$$

The first term in (3.8) vanishes by integration by parts, $3 \langle u_x u^2 \rangle = \langle (u^3)_x \rangle = 0$, and integrating the third term by parts yet again, one gets [22] that the energy variation

$$(3.9) \quad \dot{E} = P - D, \quad P = \langle u_x^2 \rangle, \quad D = \langle u_{xx}^2 \rangle$$

balances the power P pumped in by antidiffusion u_{xx} against the energy dissipation rate D by hyperviscosity u_{xxxx} in the KS equation (2.1).

The time averaged energy density \overline{E} computed on a typical orbit goes to a constant, so the mean values (3.2) of drive and dissipation exactly balance each other:

$$(3.10) \quad \overline{\dot{E}} = \lim_{t \rightarrow \infty} \frac{1}{t} \int_0^t d\tau \dot{E} = \overline{P} - \overline{D} = 0.$$

In particular, the equilibria and relative equilibria fall onto the diagonal in Figure 14(a), and so do time averages computed on periodic orbits and relative periodic orbits:

$$(3.11) \quad \overline{E}_p = \frac{1}{T_p} \int_0^{T_p} d\tau E(\tau), \quad \overline{P}_p = \frac{1}{T_p} \int_0^{T_p} d\tau P(\tau) = \overline{D}_p.$$

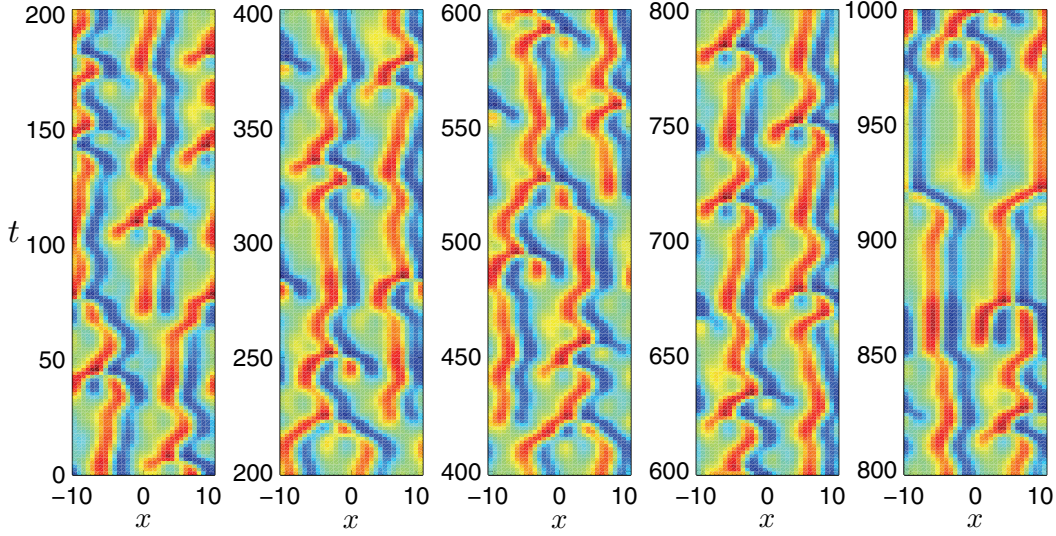


Figure 4. A typical chaotic orbit of the KS flow, system size $L = 22$.

In the Fourier basis (3.7) the conservation of energy on average takes the form

$$(3.12) \quad 0 = \sum_{k=-\infty}^{\infty} (q_k^2 - q_k^4) \overline{E}_k, \quad E_k(t) = \frac{1}{2} |a_k(t)|^2.$$

The large k convergence of this series is insensitive to the system size L ; \overline{E}_k have to decrease much faster than q_k^{-4} . Deviation of E_k from this bound for small k determines the active modes. For equilibria an L -independent bound on E is given by Michelson [42]. The best current bound [17, 3] on the long-time limit of E as a function of the system size L scales as $E \propto L^2$.

4. Geometry of state space with $L = 22$. We now turn to exploring Hopf’s vision numerically, on a specific KS system. An instructive example is offered by the dynamics for the $L = 22$ system to which we specialize for the rest of this paper. The size of this small system is ~ 2.5 mean wavelengths ($\tilde{L}/\sqrt{2} = 2.4758\dots$), and the competition between states with wavenumbers 2 and 3 leads to what, in the context of boundary shear flows, would be called [23] the “empirically observed sustained turbulence,” but in the present context may equally well be characterized as a “chaotic attractor.” A typical long orbit is shown in Figure 4. Asymptotic attractor structure of small systems like the one studied here is very sensitive to system parameter variations, and, as is true of any realistic unsteady flow, there is no rigorous way of establishing that this turbulence is sustained for all time, rather than being merely a very long transient on its way to an attracting periodic state. For large system size, as shown in Figure 1, it is hard to imagine a scenario under which attracting periodic states (as shown in [16], they do exist) would have significantly large immediate basins of attraction. Regardless of the (non)existence of a $t \rightarrow \infty$ chaotic attractor, study of the invariant unstable solutions and the associated Smale horseshoe structures in a system’s state space offers valuable insights into the observed unstable “coherent structures.”

Because of the strong k^4 contraction, for a small system size the long-time dynamics is confined to a low-dimensional inertial manifold [29]. Indeed, numerically the covariant Lyapunov vectors [20] of the $L = 22$ chaotic attractor separate into eight “physical” vectors with small Lyapunov exponents $(\lambda_j) = (0.048, 0, 0, -0.003, -0.189, -0.256, -0.290, -0.310)$ and the remaining 54 “hyperbolically isolated” vectors with rapidly decreasing exponents $(\lambda_j) = (-1.963, -1.967, -5.605, -5.605, -11.923, -11.923, \dots) \approx -(j/\tilde{L})^4$, in full agreement with the investigations by Yang et al. [49] of KS equations for large system sizes. The chaotic dynamics mostly takes place close to a 8-dimensional manifold, with strong contraction in other dimensions. The two zero exponents are due to the time and space translational symmetries of the KS equation, and the two corresponding dimensions can be quotiented out by means of discrete-time Poincaré sections and $O(2)$ group orbit slices. It was shown in [6, 38] that within unstable-manifold curvilinear coordinate frames, the dynamics on the attractor can sometimes be well approximated by local 1- or 2-dimensional Poincaré return maps. Hence a relatively small number of real Fourier modes, such as the 62 to 126 used in calculations presented here, suffices to obtain invariant solutions numerically accurate to within 10^{-5} .

We next investigate the properties of equilibria and relative equilibria and determine numerically a large set of the short period relative periodic orbits for KS in a periodic cell of size $L = 22$.

5. Equilibria and relative equilibria for $L = 22$. In addition to the trivial equilibrium $u = 0$ (denoted E_0), we find three equilibria with dominant wavenumber k (denoted E_k) for $k = 1, 2, 3$. All equilibria, shown in Figure 3, are symmetric with respect to the reflection symmetry (2.5). In addition, E_2 and E_3 are symmetric with respect to translation (2.12), by $L/2$ and $L/3$, respectively. E_2 and E_3 essentially lie in the 2nd and 3rd Fourier component complex planes, with small deformations of the $k = 2j$ and $k = 3j$ harmonics, respectively.

The stability of the equilibria is characterized by the eigenvalues λ_j of the stability matrix. The leading 10 eigenvalues for each equilibrium are listed in Table 1; those with $\mu > -2.5$ are also plotted in Figure 5. We have computed (available upon request) the corresponding eigenvectors as well. As an equilibrium with $\text{Re } \lambda_j > 0$ is unstable in the direction of the corresponding eigenvector $\mathbf{e}^{(j)}$, the eigenvectors provide flow-intrinsic (PDE discretization-independent) coordinates which we use for visualization of unstable manifolds and homo/heteroclinic connections between equilibria. We find such coordinate frames, introduced by Gibson and coworkers [19, 18], better suited to visualization of nontrivial solutions than the more standard Fourier mode (eigenvectors of the $u(x, t) = 0$ solution) projections.

The eigenvalues of E_0 are determined by the linear part of the KS equation (B.4): $\lambda_k = (k/\tilde{L})^2 - (k/\tilde{L})^4$. For $L = 22$, there are three pairs of unstable eigenvalues, corresponding, in decreasing order, to three unstable modes $k = 2, 3$, and 1. For each mode, the corresponding eigenvectors lie in the plane spanned by $\text{Re } a_k$ and $\text{Im } a_k$. Table 1 lists the symmetries of the stability eigenvectors of equilibria E_1 to E_3 .

Consistent with the bifurcation diagram of Figure 2, we find two pairs of relative equilibria (2.15) with velocities $c = \pm 0.73699$ and ± 0.34954 , which we label $\text{TW}_{\pm 1}$ and $\text{TW}_{\pm 2}$, for “traveling waves.” The profiles of the two relative equilibria and their time evolution with eventual decay into the chaotic attractor are shown in Figure 6. The leading eigenvalues of $\text{TW}_{\pm 1}$ and $\text{TW}_{\pm 2}$ are listed in Table 1.

Table 1

Leading eigenvalues $\lambda_j = \mu_j \pm i\nu_j$ and symmetries of the corresponding eigenvectors of KS equilibria and relative equilibria for $L = 22$ system size. We have used as our reference states those that lie within the antisymmetric subspace \mathbb{U}^+ , and also listed the symmetries of the $L/4$ translated ones.

E_1	μ_j	ν_j	Symmetry	$\tau_{1/4}E_n$	Symmetry
$\lambda_{1,2}$	0.1308	0.3341	-	-	-
$\lambda_{3,4}$	0.0824	0.3402	\mathbb{U}^+	$\mathbb{U}^{(1)}$	
λ_5	0		-	-	-
$\lambda_{6,7}$	-0.2287	0.1963	\mathbb{U}^+	$\mathbb{U}^{(1)}$	
λ_8	-0.2455		-	-	-
λ_9	-2.0554		\mathbb{U}^+	$\mathbb{U}^{(1)}$	
λ_{10}	-2.0619		-	-	-
<hr/>					
E_2					
$\lambda_{1,2}$	0.1390	0.2384	\mathbb{U}^+	$\mathbb{U}^{(1)}$	
λ_3	0		$\tau_{1/2}$	$\tau_{1/2}$	
$\lambda_{4,5}$	-0.0840	0.1602	$\mathbb{U}^{(1)}$	\mathbb{U}^+	
λ_6	-0.1194		$\tau_{1/2}$	$\tau_{1/2}$	
$\lambda_{7,8}$	-0.2711	0.3563	$\mathbb{U}^+, \mathbb{U}^{(1)}, \tau_{1/2}$	$\mathbb{U}^+, \mathbb{U}^{(1)}, \tau_{1/2}$	
λ_9	-2.0130		$\mathbb{U}^{(1)}$	\mathbb{U}^+	
λ_{10}	-2.0378		\mathbb{U}^+	$\mathbb{U}^{(1)}$	
<hr/>					
E_3					
λ_1	0.0933		\mathbb{U}^+	$\mathbb{U}^{(1)}$	
λ_2	0.0933		-	-	
λ_3	0		$\tau_{1/3}$	$\tau_{1/3}$	
λ_4	-0.4128		$\mathbb{U}^+, \tau_{1/3}$	$\mathbb{U}^{(1)}, \tau_{1/3}$	
$\lambda_{5,6}$	-0.6108	0.3759	\mathbb{U}^+	$\mathbb{U}^{(1)}$	
$\lambda_{7,8}$	-0.6108	0.3759	-	-	
λ_9	-1.6641		-	-	
λ_{10}	-1.6641		\mathbb{U}^+	$\mathbb{U}^{(1)}$	
<hr/>					
$TW_{\pm 1}$					
$\lambda_{1,2}$	0.1156	0.8173	-	-	
$\lambda_{3,4}$	0.0337	0.4189	-	-	
λ_5	0		-	-	
λ_6	-0.2457		-	-	
$\lambda_{7,8}$	-0.3213	0.9813	-	-	
<hr/>					
$TW_{\pm 2}$					
λ_1	0.3370		-	-	
λ_2	0		-	-	
$\lambda_{3,4}$	-0.0096	0.6288	-	-	
$\lambda_{5,6}$	-0.2619	0.5591	-	-	
$\lambda_{7,8}$	-0.3067	0.0725	-	-	

Table 2 lists equilibrium energy E , the local Poincaré section return time T , radially expanding Floquet multiplier Λ_e , and the least contracting Floquet multiplier Λ_c for all $L = 22$ equilibria and relative equilibria. The return time $T = 2\pi/\nu_e$ is given by the imaginary part of the leading complex eigenvalue, the expansion multiplier per one turn of the most unstable spiral-out by $\Lambda_e \approx \exp(\mu_e T)$, and the contraction rate along the slowest contracting stable

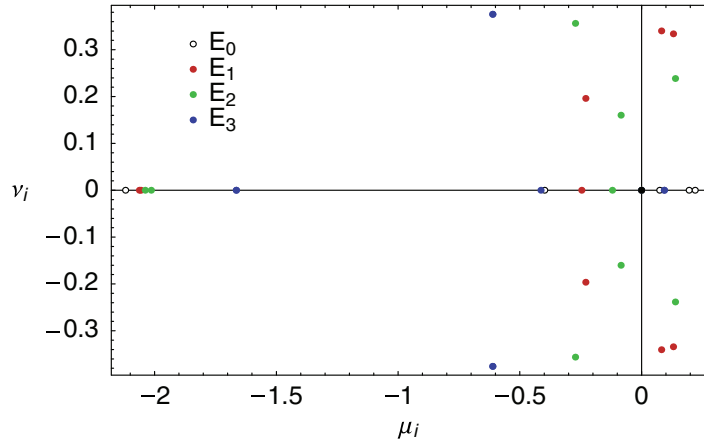


Figure 5. Leading equilibrium stability eigenvalues, $L = 22$ system size.

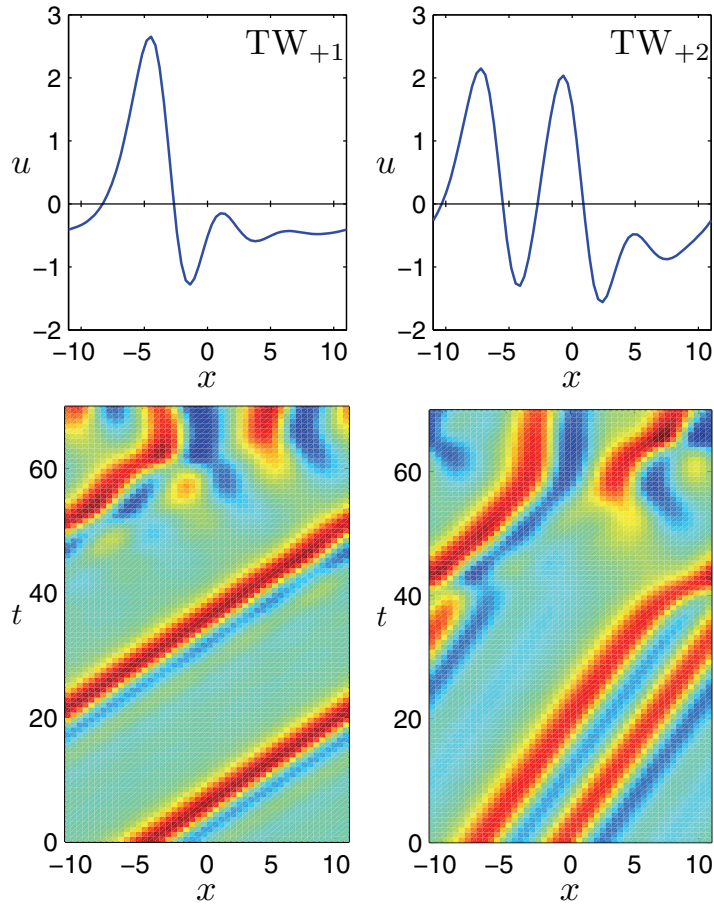


Figure 6. Relative equilibria: TW_{+1} with velocity $c = 0.737$ and TW_{+2} with velocity $c = 0.350$. The upper panels show the relative equilibria profiles. The lower panels show evolution of slightly perturbed relative equilibria and their decay into generic turbulence. Each relative equilibrium has a reflection symmetric partner related by $u(x) \rightarrow -u(-x)$ traveling with velocity $-c$.

Table 2

Properties of equilibria and relative equilibria determining the system dynamics in their vicinity. T is the characteristic time scale of the dynamics, Λ_e and Λ_c are the leading expansion and contraction multipliers, and E is the energy (3.6).

	E	T	Λ_e	Λ_c
E_1	0.2609	18.81	11.70	0.01
E_2	0.4382	26.35	39.00	0.11
E_3	1.5876	10.72	2.72	0.01
$TW_{\pm 1}$	0.4649	7.69	2.43	0.15
$TW_{\pm 2}$	0.6048	2.97	2.72	0.97

eigendirection by $\Lambda_c \approx \exp(\mu_c T)$. For E_3 and $TW_{\pm 2}$, whose leading eigenvalues are real, we use $T = 1/\lambda_1$ as the characteristic time scale. While the complex eigenvalues set time scales of recurrences, this time scale is useful for comparison of leading expanding and the slowest contracting multiplier. We learn that the shortest “turn-over” time is $\approx 10 - 20$, and that if there exist horseshoe sets of unstable periodic orbits associated with these equilibria, they have unstable multipliers of order of $\Lambda_e \sim 5 - 10$, and that they are surprisingly thin in the folding direction, with contracting multipliers of order of 10^{-2} , as also observed in [38].

5.1. Unstable manifolds of equilibria and their heteroclinic connections. As shown in Table 1, the E_1 equilibrium has two unstable planes within which the solutions are spiralling out (that is, two pairs of complex conjugate eigenvalues). The E_2 has one such plane, while the E_3 has two real positive eigenvalues, so the solutions are moving radially away from the equilibrium within the plane spanned by the corresponding eigenvectors. Since E_1 has a larger unstable subspace, it is expected to have much less influence on the long-time dynamics compared to E_2 and E_3 .

Many methods have been developed for visualization of stable and unstable manifolds; see [33] for a survey. For high-dimensional contracting flows, visualization of stable manifolds is impossible, unless the system can be restricted to an approximate low-dimensional inertial manifold, as, for example, in [28]. The unstable manifold visualization also becomes harder as its dimension increases. Here we concentrate on visualizations of 1- and 2-dimensional unstable manifolds. Our visualization is unsophisticated compared to the methods of [33], yet sufficient for our purposes since, as we shall see, the unstable manifolds we study terminate in another equilibrium, and thus there is no need to track them for long times.

To construct an invariant manifold containing solutions corresponding to the pair of unstable complex conjugate eigenvalues, $\lambda = \mu \pm i\nu$, $\mu > 0$, we start with a set of initial conditions near equilibrium E_k ,

$$(5.1) \quad a(0) = a_{E_k} + \epsilon \exp(\delta) \mathbf{e}^{(j)},$$

where δ takes a set of values uniformly distributed in the interval $[0, 2\pi\mu/\nu]$, $\mathbf{e}^{(j)}$ is a unit vector in the unstable plane, and $\epsilon > 0$ is small.

The manifold starting within the first unstable plane of E_1 , with eigenvalues $0.1308 \pm i0.3341$, is shown in Figure 7. It appears to fall directly into the chaotic attractor. The behavior of the manifold starting within the second unstable plane of E_1 , eigenvalues $0.0824 \pm i0.3402$, is remarkably different: As can be seen in Figure 8, almost all orbits within the

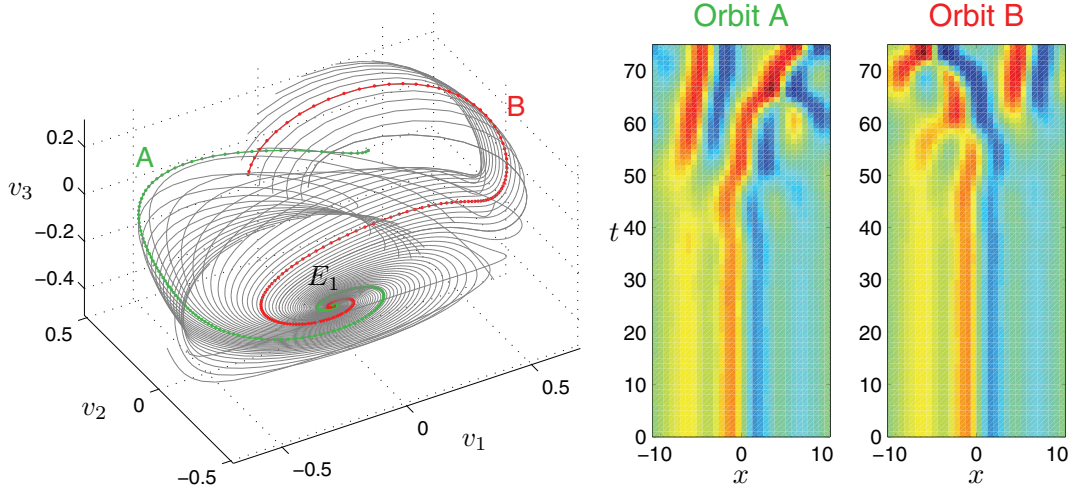


Figure 7. The left panel shows the unstable manifold of equilibrium E_1 starting within the plane corresponding to the first pair of unstable eigenvalues. The coordinate axes v_1 , v_2 , and v_3 are projections onto three orthonormal vectors \mathbf{v}_1 , \mathbf{v}_2 , and \mathbf{v}_3 , respectively, constructed from vectors $\text{Re}\mathbf{e}^{(1)}$, $\text{Im}\mathbf{e}^{(1)}$, and $\text{Re}\mathbf{e}^{(6)}$ by Gram-Schmidt orthogonalization. The right panel shows spatial representation of two orbits A and B. The change of color from blue to red indicates increasing values of $u(x)$, as in the colorbar of Figure 1.

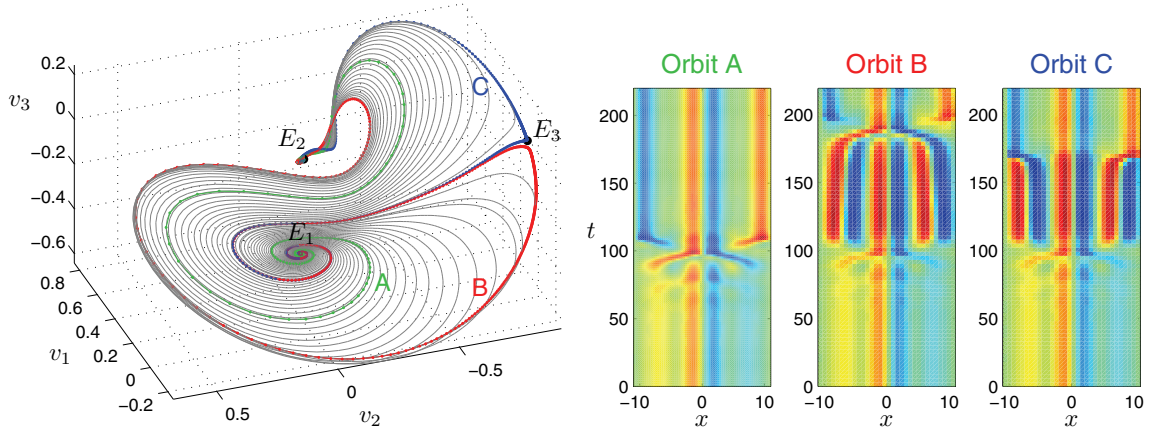


Figure 8. The left panel shows the unstable manifold of equilibrium E_1 starting within the plane corresponding to the second pair of unstable eigenvalues. The coordinate axes v_1 , v_2 , and v_3 are projections onto three orthonormal vectors \mathbf{v}_1 , \mathbf{v}_2 , and \mathbf{v}_3 , respectively, constructed from vectors $\text{Re}\mathbf{e}^{(3)}$, $\text{Im}\mathbf{e}^{(3)}$, and $\text{Re}\mathbf{e}^{(6)}$ by Gram-Schmidt orthogonalization. The right panel shows spatial representation of three orbits. Orbits B and C pass close to the equilibrium E_3 .

manifold converge to the equilibrium E_2 . The manifold also contains a heteroclinic connection from E_1 to E_3 , and is bordered by the λ_1 -eigendirection unstable manifold of E_3 .

The 2-dimensional unstable manifold of E_2 is shown in Figure 9. All orbits within the manifold, except for the heteroclinic connections from E_2 to E_3 , converge to E_2 shifted by $L/4$, so this manifold, minus the heteroclinic connections, can be viewed as a homoclinic connection.

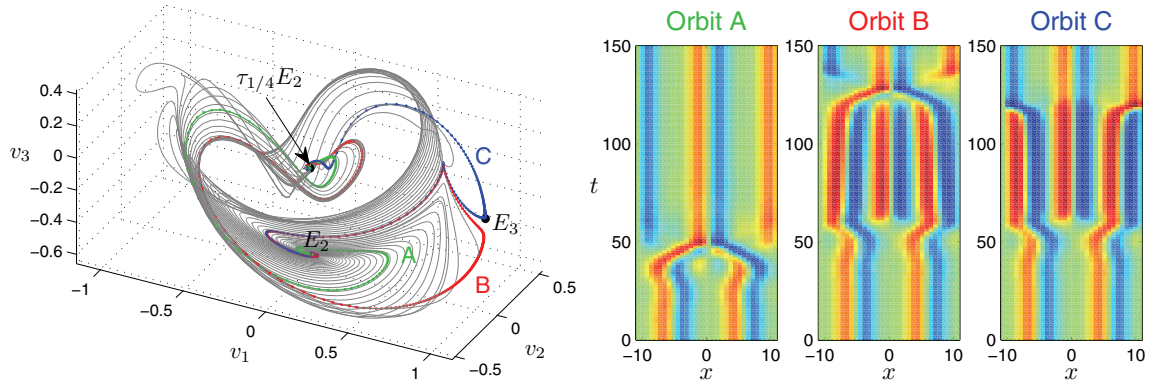


Figure 9. The left panel shows the 2-dimensional unstable manifold of equilibrium E_2 . The coordinate axes v_1 , v_2 , and v_3 are projections onto three orthonormal vectors \mathbf{v}_1 , \mathbf{v}_2 , and \mathbf{v}_3 , respectively, constructed from vectors $\text{Re} \mathbf{e}^{(1)}$, $\text{Im} \mathbf{e}^{(1)}$, and $\text{Re} \mathbf{e}^{(7)}$ by Gram–Schmidt orthogonalization. The right panel shows spatial representation of three orbits. Orbits B and C pass close to the equilibrium E_3 . See Figure 10 for a different visualization.

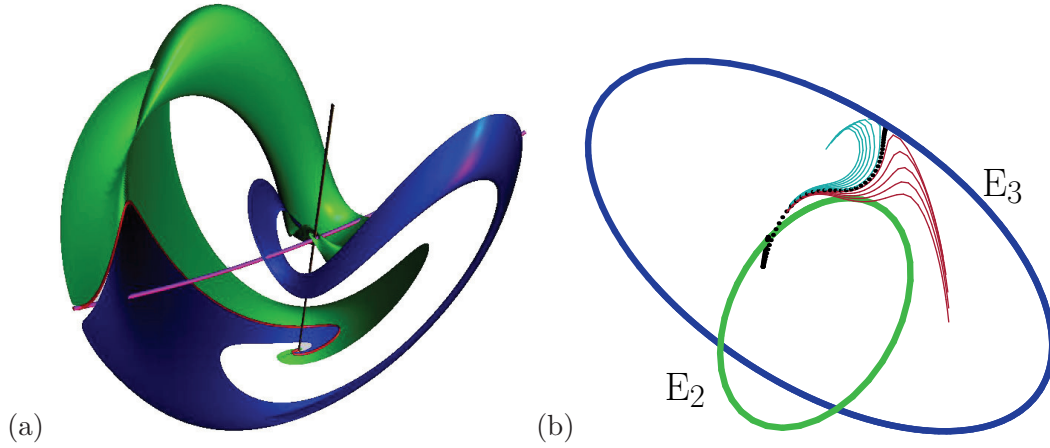


Figure 10. (a) (blue/green) The unstable manifold of the E_2 equilibrium, projection in the coordinate axes of Figure 9. (black line) The circle of E_2 equilibria related by the translation invariance. (purple line) The circle of E_3 equilibria. (red) The heteroclinic connection from the E_2 equilibrium to the E_3 equilibrium splits the manifold into two parts, colored blue and green. (b) E_2 equilibrium to E_3 equilibrium heteroclinic connection, $(\text{Re} \mathbf{e}^{(2)}, \text{Re} \mathbf{e}^{(3)}, (\text{Im} \mathbf{e}^{(2)} + \text{Im} \mathbf{e}^{(3)})/\sqrt{2})$ projection. Here we omit the unstable manifold of E_2 , keeping only a few neighboring trajectories in order to indicate the unstable manifold of E_3 . The E_2 and E_3 families of equilibria arising from the continuous translational symmetry of the KS equation on a periodic domain are indicated by the two circles.

The equilibrium E_3 has a pair of real unstable eigenvalues equal to each other. Therefore, within the plane spanned by the corresponding eigenvectors, the orbits move radially away from the equilibrium. In order to trace out the unstable manifold, we start with a set of initial conditions within the unstable plane,

$$(5.2) \quad a(0) = a_{E_3} + \epsilon(\mathbf{v}_1 \cos \phi + \mathbf{v}_2 \sin \phi), \quad \phi \in [0, 2\pi],$$

where \mathbf{v}_1 and \mathbf{v}_2 are orthonormal vectors within the plane spanned by the two unstable

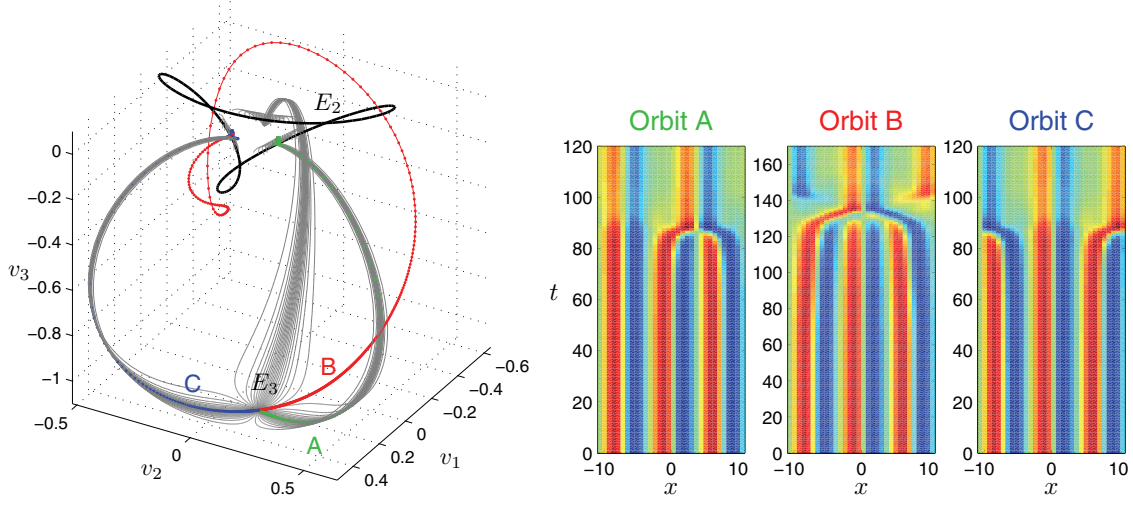


Figure 11. The left panel shows the 2-dimensional unstable manifold of equilibrium E_3 . The coordinate axes v_1 , v_2 , and v_3 are projections onto three orthonormal vectors \mathbf{v}_1 , \mathbf{v}_2 , and \mathbf{v}_3 , respectively, constructed from vectors $\mathbf{e}^{(1)}$, $\mathbf{e}^{(2)}$, and $\mathbf{e}^{(4)}$ by Gram–Schmidt orthogonalization. The black line shows a family of E_2 equilibria related by translational symmetry. The right panel shows spatial representation of three orbits. Orbits B and C are two different heteroclinic orbits connecting E_3 to the same point on the E_2 line.

eigenvectors. The unstable manifold of E_3 is shown in Figure 11. The 3-fold symmetry of the manifold is related to the symmetry of E_3 with respect to translation by $L/3$. The manifold contains heteroclinic orbits connecting E_3 to three different points of the circle of equilibria E_2 translated set of solutions. Note also that the segments of orbits B and C between E_3 and E_2 in Figures 8 and 9 represent the same heteroclinic connections as orbits B and C in Figure 11.

Heteroclinic connections are nongeneric for high-dimensional systems, but can be robust in systems with continuous symmetry; see [35] for a review. Armbruster, Guckenheimer, and Holmes [2] study a fourth order truncation of KS dynamics on the center-unstable manifold of E_2 close to a bifurcation off the constant $u(x, t) = 0$ solution and prove existence of a heteroclinic connection; see also [1]. Kevrekidis, Nicolaenko, and Scovel [32] study the dynamics numerically and establish the existence of a robust heteroclinic connection for a range of parameters close to the onset of the 2-cell branch in terms of the symmetry and a flow invariant subspace. We adopt their arguments to explain the new heteroclinic connections shown in Figure 12 that we have found for $L = 22$. For our system size there are exactly two representatives of the E_2 family that lie in the intersection of \mathcal{U}^+ and $\mathcal{U}^{(1)}$ related to each other by an $L/4$ shift. Denote them by E_2 and $\tau_{1/4}E_2$, respectively. The unstable eigenplane of E_2 lies on \mathcal{U}^+ , while that of $\tau_{1/4}E_2$ lies on $\mathcal{U}^{(1)}$; cf. Table 1. The E_3 family members that live in \mathcal{U}^+ have one of their unstable eigenvectors (the one related to the heteroclinic connection to the E_2 family) on \mathcal{U}^+ , while the other does not lie on symmetry invariant subspace. Similarly, for the E_1 family we observe that the equilibria in \mathcal{U}^+ have an unstable plane on \mathcal{U}^+ (again related to the heteroclinic connection) and a second one with no symmetry. Thus $\tau_{1/4}E_2$ appears as a sink on \mathcal{U}^+ , while all other equilibria appear as sources. This explains the heteroclinic connections from E_1 , E_2 , and E_3 to $\tau_{1/4}E_2$. Observing that $\tau_{1/4}\mathcal{U}^+ = \mathcal{U}^{(1)}$ and

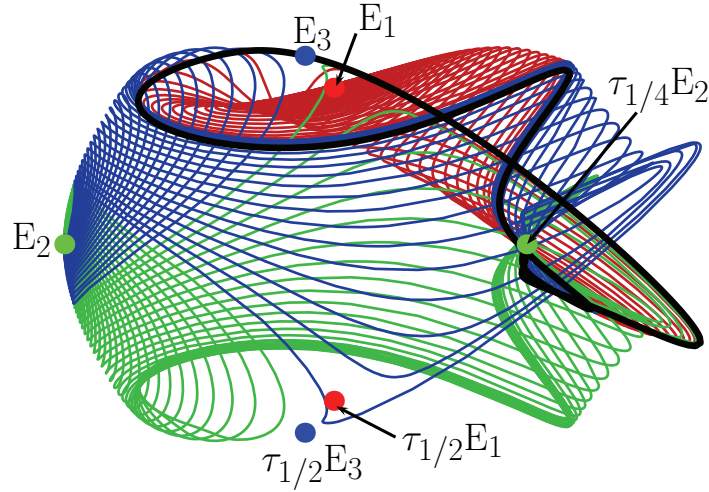


Figure 12. Heteroclinic connections on \mathbb{U}^+ : (red) The unstable manifold of E_1 equilibrium. (blue/green) The unstable manifold of E_2 equilibrium. (black) Heteroclinic connections from the E_3 equilibrium to the $\tau_{1/4}E_2$ equilibrium, where $\tau_{1/m}u(x) = u(x + L/m)$ is a rational shift (2.6). Projection from 128 dimensions onto the plane given by the vectors $a_{E_2} - a_{\tau_{1/4}E_2}$ and $a_{E_3} - a_{\tau_{1/2}E_3}$.

taking into account Table 1, we understand that within $\mathbb{U}^{(1)}$ we have connections from $\tau_{1/4}E_2$ (and members of E_1 and E_3 families) to E_2 and the formation of a heteroclinic loop. Due to the translational invariance of the KS system there is a heteroclinic loop for any two points of the E_2 family related by an $\tau_{1/4}$ -shift.

6. Relative periodic orbits for $L = 22$. The relative periodic orbits satisfy the condition (2.20), $u(x + \ell_p, T_p) = u(x, 0)$, where T_p is the period and ℓ_p the phase shift. We have limited our search to orbits with $T_p < 200$ and found over 30,000 relative periodic orbits with $\ell_p > 0$. The details of the algorithm used and the search strategy employed are given in Appendix C. Each relative periodic orbit with phase shift $\ell_p > 0$ has a reflection symmetric partner $u_p(x) \rightarrow -u_p(-x)$ with phase shift $-\ell_p$.

The small period relative periodic orbits outline the coarse structure of the chaotic attractor, while the longer period relative periodic orbits resolve the finer details of the dynamics. The first four orbits with the shortest periods we have found are shown in Figure 13(a)–(d). The shortest relative periodic orbit with $T_p = 16.4$ is also the most unstable, with one positive Floquet exponent equal to 0.328. The other short orbits are less unstable, with the largest Floquet exponent in the range 0.018–0.073, typical of the long-time attractor average.

We have found relative periodic orbits which stay close to the unstable manifold of E_2 . As is illustrated in Figure 13(e)–(h), all such orbits have shift $\ell_p \approx L/4$, similar to the shift of orbits within the unstable manifold of E_2 , which start at E_2 and converge to $\tau_{1/4}E_2$ (see Figure 9). This confirms that the cage of unstable manifolds of equilibria plays an important role in organizing the chaotic dynamics of the KS equation.

7. Preperiodic orbits. As discussed in section 2.3, a relative periodic orbit will be periodic, that is, $\ell_p = 0$, if it either (a) lives within the \mathbb{U}^+ antisymmetric subspace, $-u(-x, 0) = u(x, 0)$, or (b) returns to its reflection or its discrete rotation after a period, $u(x, t + T_p) = \gamma u(x, t)$,

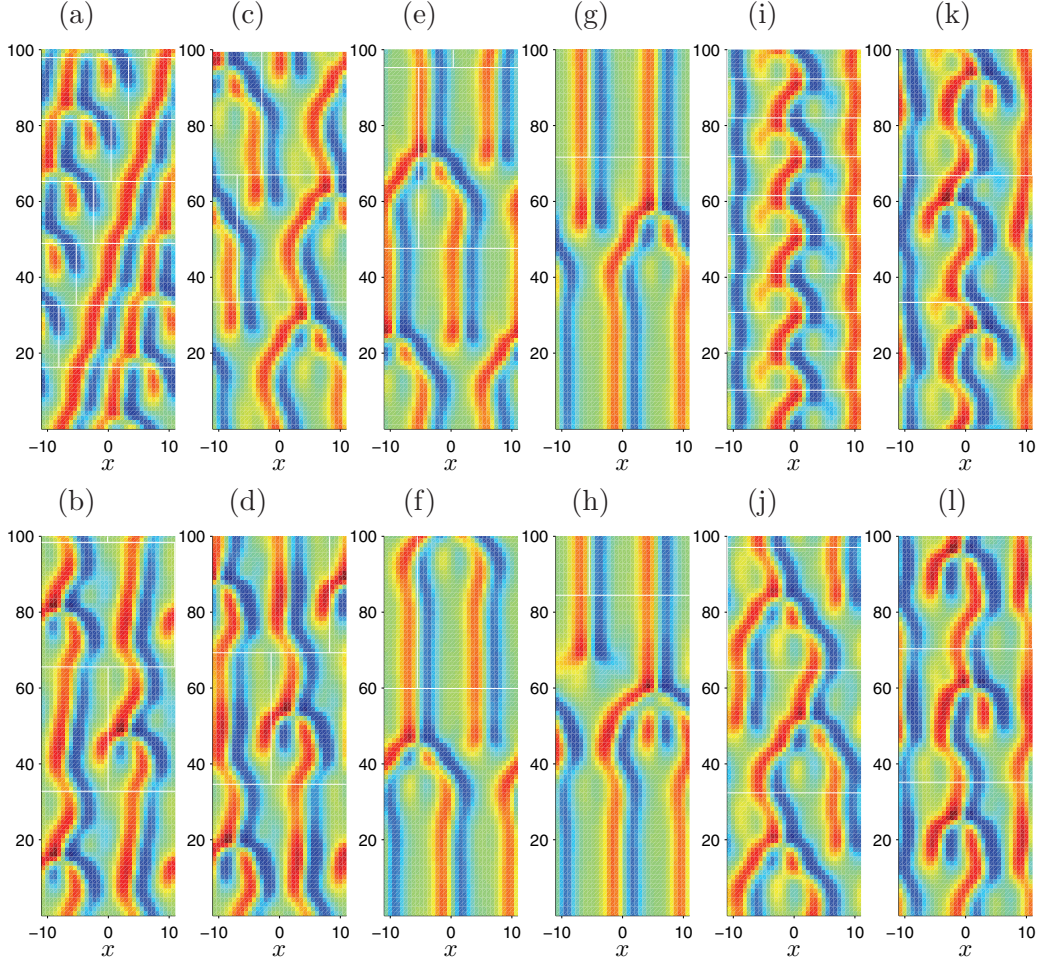


Figure 13. Selected relative periodic and preperiodic orbits of KS flow with $L = 22$: (a) $T_p = 16.3$, $\ell_p = 2.86$; (b) $T_p = 32.8$, $\ell_p = 10.96$; (c) $T_p = 33.5$, $\ell_p = 4.04$; (d) $T_p = 34.6$, $\ell_p = 9.60$; (e) $T_p = 47.6$, $\ell_p = 5.68$; (f) $T_p = 59.9$, $\ell_p = 5.44$; (g) $T_p = 71.7$, $\ell_p = 5.503$; (h) $T_p = 84.4$, $\ell_p = 5.513$; (i) $T_p = 10.3$; (j) $T_p = 32.4$; (k) $T_p = 33.4$; (l) $T_p = 35.2$. Horizontal and vertical white lines indicate periodicity and phase shift of the orbits, respectively.

$\gamma^m = e$, and is thus periodic with period mT_p . The dynamics of KS flow in the antisymmetric subspace and periodic orbits with symmetry (a) have been investigated previously [6, 37, 38]. The KS flow does not have any periodic orbits of this type for $L = 22$.

Using the algorithm and strategy described in Appendix C, we have found over 30,000 preperiodic orbits with $T_p < 200$ which possess symmetry of type (b) with $\gamma = R \in D_1$. Some of the shortest such orbits that we have found are shown in Figure 13(i)–(l). Several were found as repeats of preperiodic orbits during searches for relative periodic orbits with nonzero shifts, while most have been found as solutions of the preperiodic orbit condition (2.21) with reflection, which takes the form

$$(7.1) \quad -\mathbf{g}(-\ell)a^*(T_p) = a(0)$$

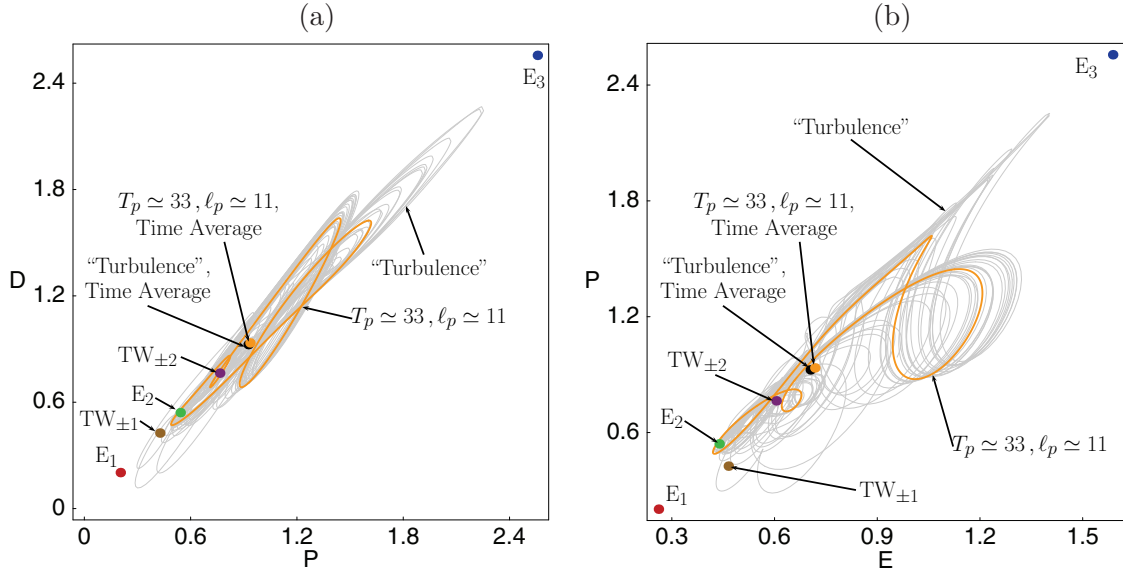


Figure 14. (a) Power input P vs. dissipation rate D , and (b) energy E vs. power input P , for several equilibria and relative equilibria, a relative periodic orbit, and a typical turbulent long-time trajectory. Projections of the heteroclinic connections are given in Figure 15. System size $L = 22$.

in the Fourier space representation (compare this to the condition (C.1) for relative periodic orbits).

8. Energy transfer rates for $L = 22$. In Figure 14 we plot (3.9), the time-dependent \dot{E} in the power input P versus dissipation rate D plane, for $L = 22$ equilibria and relative equilibria, a selected relative periodic orbit, and for a typical turbulent long-time trajectory.

Projections from the ∞ -dimensional state space onto the 3-dimensional (E, P, D) representation of the flow, such as Figures 14 and 15, can be misleading. The most one can say is that if points are clearly separated in an (E, P, D) plot (for example, in Figure 14, E_1 equilibrium is outside the recurrent set), they are also separated in the full state space. The converse is not true—states of very different topology can have similar energies.

An example is the relative periodic orbit $(T_p, \ell_p) = (32.8, 10.96)$ (see Figure 13(b)), which is the least unstable short relative periodic orbit that we have detected in this system. It appears to be well embedded within the turbulent flow. The mean power $\overline{P_p}$ evaluated as in (3.11) (see Figure 14) is numerically quite close to the long-time turbulent time average \overline{P} . Similarly close prediction of mean dissipation rate in the plane Couette flow from a single-period periodic orbit computed by Kawahara and Kida [31] has lead to optimistic hopes that turbulence is different from low-dimensional chaos, insofar as the determination of one special periodic orbit could yield all long-time averages. Regrettably, this is not true—as always, here too one needs a hierarchy of periodic orbits of increasing length to obtain accurate predictions [11].

For any given relative periodic orbit a convenient visualization is offered by the *mean velocity frame*, that is, a reference frame that rotates with velocity $c_p = \ell_p/T_p$. In the mean velocity frame a relative periodic orbit becomes a periodic orbit, as in Figure 16(b). However,

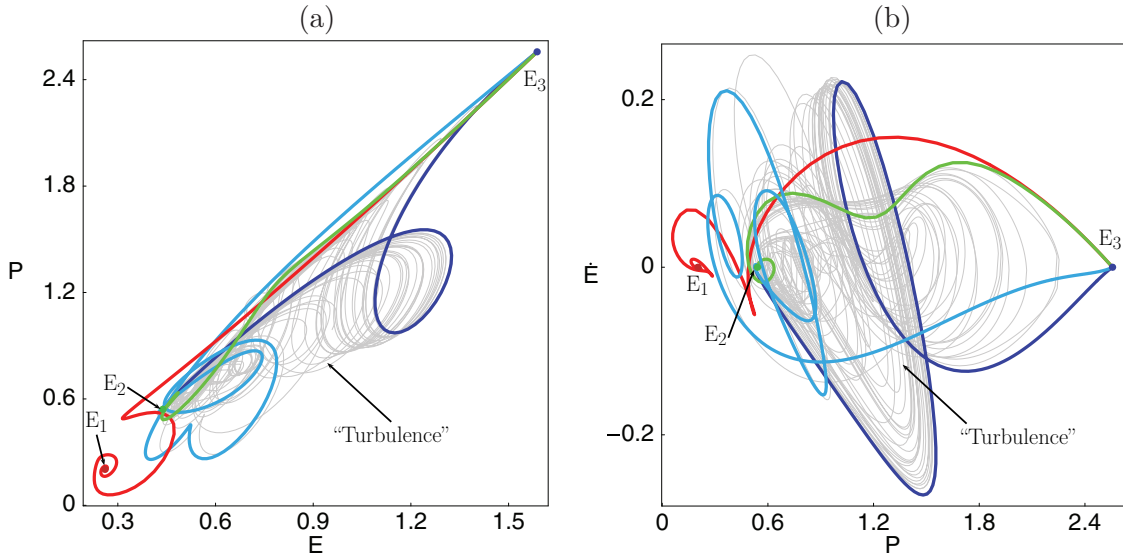


Figure 15. Two projections of the (E, P, \dot{E}) representation of the flow. E_1 (red), E_2 (green), E_3 (blue), heteroclinic connections from E_2 to E_3 (green), from E_1 to E_3 (red), and from E_3 to E_2 (shades of blue), superimposed over a generic long-time turbulent trajectory (grey). (a) As in (b), with labels omitted for clarity. (b) A plot of $\dot{E} = P - D$ yields a clearer visualization than (a). System size $L = 22$.

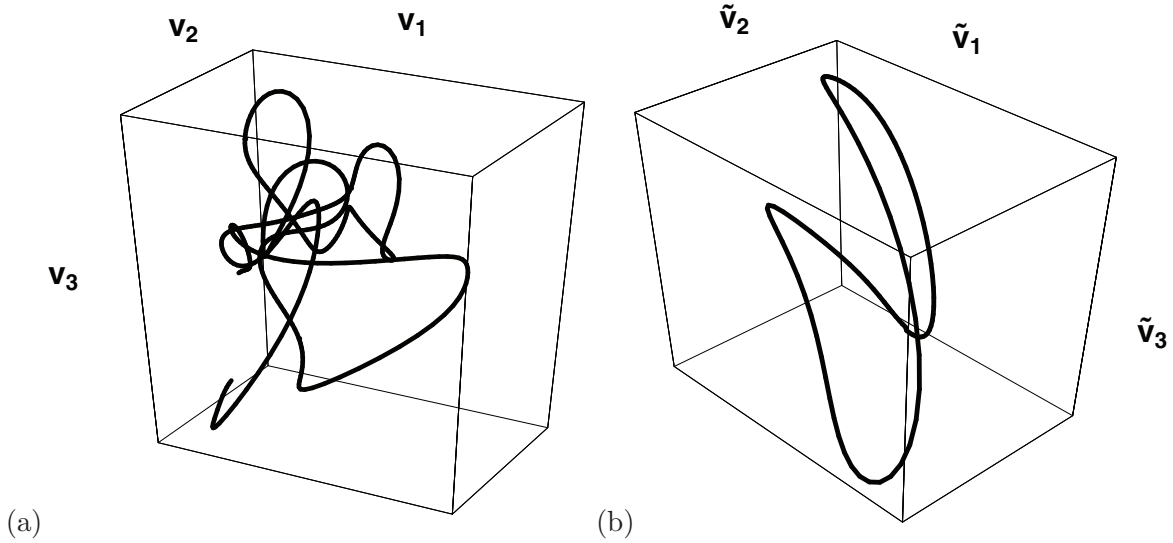


Figure 16. The relative periodic orbit with $(T_p, \ell_p) = (33.5, 4.04)$ from Figure 13(c) which appears well embedded within the turbulent flow: (a) A stationary state space projection, traced for four periods T_p . The coordinate axes v_1 , v_2 , and v_3 are those of Figure 9. (b) In the comoving mean velocity frame.

each relative periodic orbit has its own mean velocity frame, and thus sets of relative periodic orbits are difficult to visualize simultaneously.

9. Summary. In this paper we study the Kuramoto–Sivashinsky flow as a staging ground for testing dynamical systems approaches to moderate Reynolds number turbulence in full-fledged (*not* a few-modes model), infinite-dimensional state space PDE settings [25], and present a detailed geometrical portrait of dynamics in the KS state space for the $L = 22$ system size, the smallest system size for which this system empirically exhibits “sustained turbulence.”

Compared to earlier work [6, 37, 38, 40], the main advances here are the new insights into the role that continuous symmetries, discrete symmetries, low-dimensional unstable manifolds of equilibria, and the connections between equilibria play in organizing the flow. The key new feature of the translationally invariant KS system on a periodic domain are the attendant continuous families of relative equilibria (traveling waves) and relative periodic orbits. We have now understood the preponderance of solutions of relative type, and lost fear of them: A large number of unstable relative periodic orbits and periodic orbits has been determined here numerically.

Visualization of infinite-dimensional state space flows, especially in presence of continuous symmetries, is not straightforward. At first glance, turbulent dynamics visualized in the state space appears hopelessly complex, but under a detailed examination it is much less so than feared: For strongly dissipative flows (KS, Navier–Stokes) it is pieced together from low-dimensional local unstable manifolds connected by fast transient interludes. In this paper we offer two low-dimensional visualizations of such flows: (1) projections onto 2- or 3-dimensional PDE representation-independent dynamically invariant frames, and (2) projections onto the physical, symmetry invariant but time-dependent, energy transfer rates.

Relative periodic orbits require a reformulation of the periodic orbit theory [10], as well as a rethinking of the dynamical systems approaches to constructing symbolic dynamics, outstanding problems that we hope to address in the near future [45, 44]. What we have learned from the $L = 22$ system is that many of these relative periodic orbits appear organized by the unstable manifold of E_2 , closely following the homoclinic loop formed between E_2 and $\tau_{1/4}E_2$.

In the spirit of the parallel studies of boundary shear flows [23], the KS system size of $L = 22$ was chosen as the smallest system size for which KS empirically exhibits “sustained turbulence.” This is convenient both for the analysis of the state space geometry, and for the numerical reasons, but the price is high—much of the observed dynamics is specific to this unphysical, externally imposed periodicity. What needs to be understood is the nature of equilibrium and relative periodic orbit solutions in the $L \rightarrow \infty$ limit, and the structure of the $L = \infty$ periodic orbit theory.

In summary, KS equilibria (and plane Couette flow; see [19]), relative equilibria, periodic orbits, and relative periodic orbits embody Hopf’s vision [26]: together they form the repertoire of recurrent spatio-temporal patterns explored by turbulent dynamics.

Appendix A. Integrating the KS equation numerically. The KS equation in terms of Fourier modes,

$$(A.1) \quad \hat{u}_k = \mathcal{F}[u]_k = \frac{1}{L} \int_0^L u(x, t) e^{-iq_k x} dx, \quad u(x, t) = \mathcal{F}^{-1}[\hat{u}] = \sum_{k \in \mathbb{Z}} \hat{u}_k e^{iq_k x},$$

is given by

$$(A.2) \quad \dot{\hat{u}}_k = (q_k^2 - q_k^4) \hat{u}_k - \frac{iq_k}{2} \mathcal{F}[(\mathcal{F}^{-1}[\hat{u}])^2]_k.$$

Since u is real, the Fourier modes are related by $\hat{u}_{-k} = \hat{u}_k^*$.

The above system is truncated as follows: The Fourier transform \mathcal{F} is replaced by its discrete equivalent

$$(A.3) \quad a_k = \mathcal{F}_N[u]_k = \sum_{n=0}^{N-1} u(x_n) e^{-iq_k x_n}, \quad u(x_n) = \mathcal{F}_N^{-1}[a]_n = \frac{1}{N} \sum_{k=0}^{N-1} a_k e^{iq_k x_n},$$

where $x_n = nL/N$ and $a_{N-k} = a_k^*$. Since $a_0 = 0$ due to Galilean invariance and setting $a_{N/2} = 0$ (assuming N is even), the number of independent variables in the truncated system is $N - 2$:

$$(A.4) \quad \dot{a}_k = v_k(a) = (q_k^2 - q_k^4) a_k - \frac{iq_k}{2} \mathcal{F}_N[(\mathcal{F}_N^{-1}[a])^2]_k,$$

where $k = 1, \dots, N/2 - 1$, although in the Fourier transform we need to use a_k over the full range of k values from 0 to $N - 1$. As $a_k \in \mathbb{C}$, (A.4) represents a system of ODEs in \mathbb{R}^{N-2} .

The discrete Fourier transform \mathcal{F}_N can be computed by FFT. In Fortran and C, the FFTW library [14] can be used.

In order to find the fundamental matrix of the solution, or compute Lyapunov exponents of the KS flow, one needs to solve the equation for a displacement vector b in the tangent space:

$$(A.5) \quad \dot{b} = \frac{\partial v(a)}{\partial a} b.$$

Since \mathcal{F}_N is a linear operator, it is easy to show that

$$(A.6) \quad \dot{b}_k = (q_k^2 - q_k^4) b_k - iq_k \mathcal{F}_N[\mathcal{F}_N^{-1}[a] \otimes \mathcal{F}_N^{-1}[b]]_k,$$

where \otimes indicates the componentwise product of two vectors; that is, $a \otimes b = \text{diag}(a) b = \text{diag}(b) a$. This equation needs to be solved simultaneously with (A.4).

Equations (A.4) and (A.6) were solved using the exponential time differencing fourth order Runge–Kutta method (ETDRK4) [7, 30].

Appendix B. Determining stability properties of equilibria, traveling waves, and relative periodic orbits. Let f^t be the flow map of the KS equation; that is, $f^t(a) = a(t)$ is the solution of (A.4) with initial condition $a(0) = a$. The stability properties of the solution $f^t(a)$ are determined by the fundamental matrix $J(a, t)$ consisting of partial derivatives of $f^t(a)$ with respect to a . Since a and f^t are complex-valued vectors, the real-valued matrix $J(a, t)$ contains partial derivatives evaluated separately with respect to the real and imaginary parts

of a , that is,

$$(B.1) \quad J(a, t) = \frac{\partial f^t(a)}{\partial a} = \begin{pmatrix} \frac{\partial f_{R,1}^t}{\partial a_{R,1}} & \frac{\partial f_{R,1}^t}{\partial a_{I,1}} & \frac{\partial f_{R,1}^t}{\partial a_{R,2}} & & \\ \frac{\partial f_{I,1}^t}{\partial a_{R,1}} & \frac{\partial f_{I,1}^t}{\partial a_{I,1}} & \frac{\partial f_{I,1}^t}{\partial a_{R,2}} & \cdots & \\ \frac{\partial f_{R,2}^t}{\partial a_{R,1}} & \frac{\partial f_{R,2}^t}{\partial a_{I,1}} & \frac{\partial f_{R,2}^t}{\partial a_{R,2}} & & \\ & \vdots & & \ddots & \end{pmatrix},$$

where $a_k = a_{R,k} + ia_{I,k}$ and $f_k^t = f_{R,k}^t + if_{I,k}^t$. The partial derivatives $\frac{\partial f^t}{\partial a_{R,j}}$ and $\frac{\partial f^t}{\partial a_{I,j}}$ are determined by solving (A.6) with initial conditions $b_k(0) = b_{N-k}(0) = 1 + 0i$ and $b_k(0) = -b_{N-k}(0) = 0 + 1i$, respectively, for $k = j$ and $b_k(0) = 0$ otherwise.

The stability of a periodic orbit with period T_p is determined by the location of eigenvalues of $J(a_p, T_p)$ with respect to the unit circle in the complex plane.

Because of the translation invariance, the stability of a relative periodic orbit is determined by the eigenvalues of the matrix $\mathbf{g}(\ell_p) J(a_p, T_p)$, where $\mathbf{g}(\ell)$ is the action of the translation operator introduced in (2.6), which in real-valued representation takes the form of a block diagonal matrix with the 2×2 blocks

$$\begin{pmatrix} \cos q_k \ell & \sin q_k \ell \\ -\sin q_k \ell & \cos q_k \ell \end{pmatrix}, \quad k = 1, 2, \dots, N/2 - 1.$$

For an equilibrium solution a_q , $f^t(a_q) = a_q$, and so the fundamental matrix $J(a_q, t)$ can be expressed in terms of the time-independent stability matrix $A(a_q)$ as follows:

$$J(a_q, t) = e^{A(a_q)t},$$

where

$$(B.2) \quad A(a_q) = \left. \frac{\partial v}{\partial a} \right|_{a=a_q}.$$

Using the real-valued representation of (B.1), the partial derivatives of $v(a)$ with respect to the real and imaginary parts of a are given by

$$(B.3) \quad \begin{aligned} \frac{\partial v_k}{\partial a_{R,j}} &= (q_k^2 - q_k^4) \delta_{kj} - iq_k \mathcal{F}_N[\mathcal{F}_N^{-1}[a] \otimes \mathcal{F}_N^{-1}[b_R^{(j)}]]_k, \\ \frac{\partial v_k}{\partial a_{I,j}} &= (q_k^2 - q_k^4) i \delta_{kj} - iq_k \mathcal{F}_N[\mathcal{F}_N^{-1}[a] \otimes \mathcal{F}_N^{-1}[b_I^{(j)}]]_k, \end{aligned}$$

where $b_R^{(j)}$ and $b_I^{(j)}$ are complex-valued vectors such that $b_{R,k}^{(j)} = b_{R,N-k}^{(j)} = 1 + 0i$ and $b_{I,k}^{(j)} = -b_{I,N-k}^{(j)} = 0 + 1i$ for $k = j$ and $b_{R,k}^{(j)} = b_{I,k}^{(j)} = 0$ otherwise. In terms of $a_{R,k}$ and $a_{I,k}$ we have

$$\begin{aligned}
\frac{\partial v_{R,k}}{\partial a_{R,j}} &= (q_k^2 - q_k^4) \delta_{kj} + q_k(a_{I,k+j} + a_{I,k-j}), \\
\frac{\partial v_{R,k}}{\partial a_{I,j}} &= -q_k(a_{R,k+j} - a_{R,k-j}), \\
\frac{\partial v_{I,k}}{\partial a_{R,j}} &= -q_k(a_{R,k+j} + a_{R,k-j}), \\
\frac{\partial v_{I,k}}{\partial a_{I,j}} &= (q_k^2 - q_k^4) \delta_{kj} - q_k(a_{I,k+j} - a_{I,k-j}),
\end{aligned}
\tag{B.4}$$

where δ_{kj} is Kronecker delta.

The stability of equilibria is characterized by the sign of the real part of the eigenvalues of $A(a_q)$. The stability of a relative equilibrium is determined in the comoving reference frame, so the fundamental matrix takes the form $\mathbf{g}(c_q t) J(a_q, t)$. The stability matrix of a relative equilibrium is thus equal to $A(a_q) + c_q \mathcal{L}$, where $\mathcal{L} = iq_k \delta_{kj}$ is the Lie algebra translation generator, which in the real-space representation takes the form $\mathcal{L} = \text{diag}(0, q_1, 0, q_2, \dots)$.

Appendix C. Levenberg–Marquardt searches for relative periodic orbits. To find relative periodic orbits of the KS flow, we use multiple shooting and the Levenberg–Marquardt (LM) algorithm implemented in the routine `lmder` from the MINPACK software package [43].

In order to find periodic orbits, a system of nonlinear algebraic equations needs to be solved. For flows, this system is underdetermined, so, traditionally, it is augmented with a constraint that restricts the search space to be transversal to the flow (otherwise, most of the popular solvers of systems of nonlinear algebraic equations, e.g., those based on Newton’s method, cannot be used). When detecting relative periodic orbits, a constraint is added for each continuous symmetry of the flow. For example, when detecting relative periodic orbits in the complex Ginzburg–Landau equation, López et al. [40] introduce three additional constraints.

Our approach differs from those used previously in that we do not introduce the constraints. Being an optimization solver, the LM algorithm has no problem with solving an underdetermined system of equations, and, even though `lmder` explicitly restricts the number of equations to be not smaller than the number of variables, the additional equations can be set identically equal to zero [8]. In fact, there is numerical evidence that, when implemented with additional constraints, the solver usually takes more steps to converge from the same seed, or fails to converge at all [8]. In what follows we give a detailed description of the algorithm and the search strategy which we have used to find a large number of relative periodic orbits defined in (2.20) and preperiodic orbits defined in (2.21).

When searching for relative periodic orbits of truncated KS equation (A.4), we need to solve the system of $N - 2$ equations

$$\mathbf{g}(\ell) f^T(a) - a = 0,
\tag{C.1}$$

with N unknowns (a, T, ℓ) , where f^t is the flow map of the KS equation. In the case of preperiodic orbits, the system has the form

$$-\mathbf{g}(-\ell) [f^T(a)]^* - a = 0
\tag{C.2}$$

(see (7.1)).

We have tried two different implementations of the multiple shooting. The emphasis was on the simplicity of the implementations, so, even though both implementations worked equally well, each of them had its own minor drawbacks.

In the first implementation, we fix the total number of steps within each shooting stage and change the numerical integrator step size h in order to adjust the total integration time to a desired value T .

Let $(\hat{a}, \hat{T}, \hat{\ell})$ be the starting guess for a relative periodic orbit obtained through a close return within a chaotic attractor (see below). We require that the initial integration step size not exceed h_0 , so we round off the number of integration steps to $n = \lceil \hat{T}/h_0 \rceil$, where $\lceil x \rceil$ denotes the nearest integer larger than x .

The integration step size is equal to $h = T/n$. With the number of shooting stages equal to m , the system in (C.1) is rewritten as follows:

$$\begin{aligned}
 (C.3) \quad & F^{(1)} = f^\tau(a^{(1)}) - a^{(2)} = 0, \\
 & F^{(2)} = f^\tau(a^{(2)}) - a^{(3)} = 0, \\
 & \dots \\
 & F^{(m-1)} = f^\tau(a^{(m-1)}) - a^{(m)} = 0, \\
 & F^{(m)} = \mathbf{g}(\ell) f^{\tau'}(a^{(m)}) - a^{(1)} = 0,
 \end{aligned}$$

where $\tau = \lfloor n/m \rfloor h$ ($\lfloor x \rfloor$ is the nearest integer smaller than x), $\tau' = nh - (m-1)\tau$, and $a^{(j)} = f^{(j-1)\tau}(a)$, $j = 1, \dots, m$. For the detection of preperiodic orbits, the last equation in (C.3) should be replaced with

$$F^{(m)} = -\mathbf{g}(-\ell)[f^{\tau'}(a^{(m)})]^* - a^{(1)} = 0.$$

With the fundamental matrix of (C.3) written as

$$(C.4) \quad J = \begin{pmatrix} \frac{\partial F^{(j)}}{\partial a^{(k)}} & \frac{\partial F^{(j)}}{\partial T} & \frac{\partial F^{(j)}}{\partial \ell} \end{pmatrix}, \quad j, k = 1, \dots, m,$$

the partial derivatives with respect to $a^{(k)}$ can be calculated using the solution of (A.6) as described in Appendix B. The partial derivatives with respect to T are given by

$$(C.5) \quad \frac{\partial F^{(j)}}{\partial T} = \begin{cases} \frac{\partial f^\tau(a^{(j)})}{\partial \tau} \frac{\partial \tau}{\partial T} = v(f^\tau(a^{(j)})) \lfloor n/m \rfloor / n, & j = 1, \dots, m-1, \\ \mathbf{g}(\ell) v(f^{\tau'}(a^{(j)})) (1 - \frac{m-1}{n} \lfloor n/m \rfloor), & j = m. \end{cases}$$

Note that, even though $\partial f^t(a)/\partial t = v(f^t(a))$, it should not be evaluated using the equation for the vector field v . The reason for this is that, since the flow f^t is approximated by a numerical solution, the derivative of the numerical solution with respect to the step size h may differ from the vector field v , especially for larger step sizes. We evaluate the derivative by a forward difference using numerical integration with step sizes h and $h + \delta$:

$$(C.6) \quad \frac{\partial f^{jh}(a)}{\partial t} = \frac{1}{j\delta} \left[f^{j(h+\delta)}(a) - f^{jh}(a) \right], \quad j \in \mathbb{Z}^+,$$

with $t = jh$ and $\delta = 10^{-7}$ for double precision calculations. Partial derivatives $\partial F^{(j)}/\partial \ell$ are all equal to zero except for $j = m$, where it is given by

$$(C.7) \quad \frac{\partial F^{(m)}}{\partial \ell} = \frac{d\mathbf{g}}{d\ell} f^{\tau'}(a^{(m)}) = \text{diag}(iq_k e^{iq_k \ell}) f^{\tau'}(a^{(m)}).$$

This fundamental matrix is supplied to `lmdcr` augmented with two rows of zeros corresponding to the two identical zeros augmenting (C.3) in order to make the number of equations formally equal to the number of variables, as discussed above.

In the second implementation, we keep h and τ fixed and vary only $\tau' = T - (m - 1)\tau$. In this case, we need to be able to determine the numerical solution of the KS equation not only at times $t_j = jh$, $j = 1, 2, \dots$, but at any intermediate time as well. We do this by a cubic polynomial interpolation through points $f^{t_j}(a)$ and $f^{t_{j+1}}(a)$ with slopes $v(f^{t_j}(a))$ and $v(f^{t_{j+1}}(a))$. The difference from the first implementation is that partial derivatives $\partial F^{(j)}/\partial T$ are zero for all $j = 1, \dots, m - 1$, except for

$$(C.8) \quad \frac{\partial F^{(m)}}{\partial T} = \mathbf{g}(\ell) v(f^{\tau'}(a^{(m)})),$$

which, for consistency, needs to be evaluated from the cubic polynomial, not from the flow equation evaluated at $f^{\tau'}(a^{(m)})$.

For detecting relative periodic orbits of the KS flow with $L = 22$, we used $N = 32$, $h = 0.25$ (or $h_0 = 0.25$ within the first implementation), and a number of shooting stages such that $\tau \approx 40.0$. While both implementations were equally successful in detecting periodic orbits of KS flow, we found the second implementation more convenient.

The following search strategy was adopted: The search for relative periodic orbits with $T \in [10, 200]$ was conducted within a rectangular region containing the chaotic attractor. To generate a seed, a random point was selected within the region, and the flow (A.4) was integrated for a transient time $t = 40$, sufficient for an orbit to settle on the attractor at some point \hat{a} . This point was taken to be the seed location. In order to find orbits with different periods, the time interval $[10, 200]$ was subdivided into windows of length 10, i.e., $[t_{\min}, t_{\max}]$, where $t_{\min} = 10j$ and $t_{\max} = 10(j + 1)$, with $j = 1, 2, \dots, 19$. To determine the seed time \hat{T} and shift $\hat{\ell}$, we located an approximate global minimum of $\|\mathbf{g}(\ell) f^t(a) - a\|$ (or of $\|-\mathbf{g}(-\ell)[f^t(a)]^* - a\|$ in the case of preperiodic orbits) as a function of $t \in [t_{\min}, t_{\max}]$ and $\ell \in (-L/2, L/2]$. We did this simply by finding the minimum value of the function on a grid of points with resolution h in time and $L/50$ in ℓ .

Approximately equal numbers of seeds were generated for the detection of relative periodic orbits and preperiodic orbits and within each time window. The hit rate, i.e., the fraction of seeds that converged to relative periodic orbits or preperiodic orbits, varied from about 70% for windows with $t_{\max} \leq 80$ to about 30% for windows with $t_{\min} \geq 160$. The total number of hits for relative periodic orbits and preperiodic orbits was over 10^6 each. Each newly found orbit was compared, after factoring out the translation and reflection symmetries, to those already detected. As the search progressed, we found fewer and fewer new orbits, with the numbers first saturating for smaller period orbits. At the end of the search we could find very few new orbits with periods $T < 120$. Thus we found over 30,000 distinct prime relative periodic orbits with $\ell > 0$ and over 30,000 distinct prime preperiodic orbits with $T < 200$.

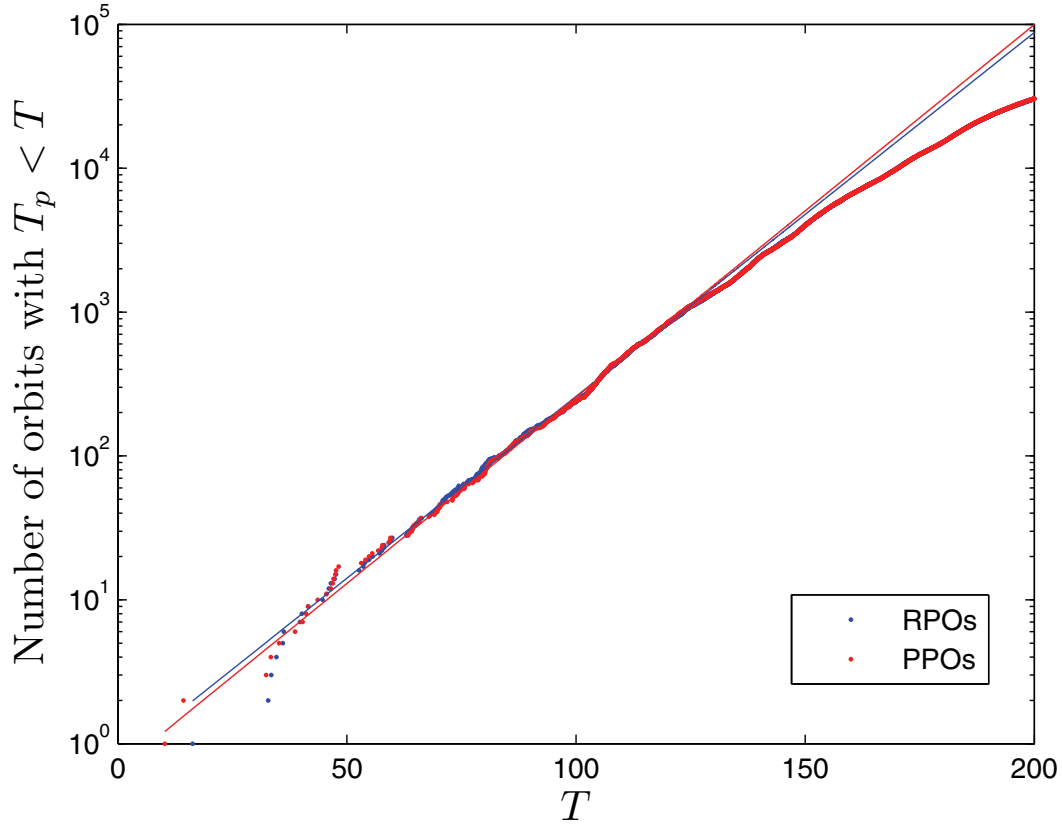


Figure 17. Numbers of detected relative periodic orbits (RPOs) and pre-periodic orbits (PPOs) with periods smaller than T . The lines indicate the linear fit to the logarithm of the number of orbits as functions of T in the range $T \in [70, 120]$.

In Figure 17 we show the numbers of detected relative periodic orbits and preperiodic orbits with periods less than T . The figure shows that the numbers of relative periodic orbits and preperiodic orbits are approximately equal and that they grow exponentially with increasing T up to $T \sim 130$, so that we are mostly missing orbits with $T > 130$. The straight line fits to the logarithm of the numbers of orbits in the interval $T \in [70, 120]$, represented by the lines in Figure 17, indicate that the total numbers of relative periodic orbits and preperiodic orbits with $T < 200$ could be over 10^5 each.

To test the structural stability of the detected orbits and their relevance to the full KS PDE, the numerical accuracy was improved by increasing the number of Fourier modes ($N = 64$) and reducing the step size ($h = 0.1$). Only a handful of orbits failed this higher-resolution test. These orbits were not included in the list of the 60,000+ orbits detected.

Acknowledgments. We are grateful to Y. Lan for pointing out to us the existence of the E_1 equilibrium at the $L = 22$ system size, J. Crofts for a key observation [8] that led to faster relative periodic orbit searches, J. F. Gibson for many spirited exchanges, and the anonymous referee for many perspicacious observations. P. C. and E. S. thank G. Robinson, Jr., for support.

REFERENCES

- [1] D. ARMBRUSTER, J. GUCKENHEIMER, AND P. HOLMES, *Heteroclinic cycles and modulated travelling waves in systems with $O(2)$ symmetry*, Phys. D, 29 (1988), pp. 257–282.
- [2] D. ARMBRUSTER, J. GUCKENHEIMER, AND P. HOLMES, *Kuramoto–Sivashinsky dynamics on the center-unstable manifold*, SIAM J. Appl. Math., 49 (1989), pp. 676–691.
- [3] J. C. BRONSKI AND T. N. GAMBILL, *Uncertainty estimates and L_2 bounds for the Kuramoto–Sivashinsky equation*, Nonlinearity, 19 (2006), pp. 2023–2039. [arXiv:math/0508481](https://arxiv.org/abs/math/0508481).
- [4] H. S. BROWN AND I. G. KEVREKIDIS, *Modulated traveling waves for the Kuramoto–Sivashinsky equation*, in Pattern Formation: Symmetry Methods and Applications, D. Benest and C. Froeschlé, eds., Fields Inst. Commun. 5, AMS, Providence, RI, 1996, pp. 45–66.
- [5] A. CHENCINER, *Three Body Problem*, Web article, 2007; online at http://scholarpedia.org/article/Three_body_problem.
- [6] F. CHRISTIANSEN, P. CVITANOVIĆ, AND V. PUTKARADZE, *Spatiotemporal chaos in terms of unstable recurrent patterns*, Nonlinearity, 10 (1997), p. 55.
- [7] S. M. COX AND P. C. MATTHEWS, *Exponential time differencing for stiff systems*, J. Comput. Phys., 176 (2002), pp. 430–455.
- [8] J. J. CROFTS, *Efficient Method for Detection of Periodic Orbits in Chaotic Maps and Flows*, Ph.D. thesis, University of Leicester, Leicester, UK, 2007. [arXiv:nlin.CD/0706.1940](https://arxiv.org/abs/nlin.CD/0706.1940).
- [9] M. C. CROSS AND P. C. HOHENBERG, *Pattern formation outside of equilibrium*, Rev. Mod. Phys, 65 (1993), p. 851.
- [10] P. CVITANOVIĆ, *Continuous symmetry reduced trace formulas*, in Chaos: Classical and Quantum, P. Cvitanović, R. Artuso, R. Mainieri, G. Tanner, and G. Vattay, eds., Web book, Niels Bohr Institute, Copenhagen, Denmark, <http://ChaosBook.org/~predrag/papers/trace.pdf>, 2007.
- [11] P. CVITANOVIĆ, R. ARTUSO, R. MAINIERI, G. TANNER, AND G. VATTAY, *Chaos: Classical and Quantum*, Niels Bohr Institute, Copenhagen, 2008; <http://ChaosBook.org/version12>.
- [12] P. CVITANOVIĆ AND B. ECKHARDT, *Symmetry decomposition of chaotic dynamics*, Nonlinearity, 6 (1993), p. 277. [arXiv:chao-dyn/9303016](https://arxiv.org/abs/chao-dyn/9303016).
- [13] C. FOIAS, B. NICOLAENKO, G. R. SELL, AND R. TEMAM, *Inertial manifold for the Kuramoto–Sivashinsky equation*, C. R. Acad. Sci. Paris Ser. I, 301 (1985), pp. 285–288.
- [14] M. FRIGO AND S. G. JOHNSON, *The design and implementation of FFTW3*, Proc. IEEE, 93 (2005), pp. 216–231.
- [15] U. FRISCH, *Turbulence*, Cambridge University Press, Cambridge, UK, 1996.
- [16] U. FRISCH, Z. S. SHE, AND O. THUAL, *Viscoelastic behavior of cellular solutions to the Kuramoto–Sivashinsky model*, J. Fluid Mech., 168 (1986), pp. 221–240.
- [17] L. GIACOMELLI AND F. OTTO, *New bounds for the Kuramoto–Sivashinsky equation*, Comm. Pure Appl. Math., 58 (2005), pp. 297–318.
- [18] J. F. GIBSON, *Movies of Plane Couette*, Technical report, Georgia Institute of Technology, Atlanta, GA, 2008, online at <http://ChaosBook.org/tutorials>.
- [19] J. F. GIBSON, J. HALCROW, AND P. CVITANOVIĆ, *Visualizing the geometry of state-space in plane Couette flow*, J. Fluid Mech., 611 (2008), pp. 107–130. [arXiv:0705.3957](https://arxiv.org/abs/0705.3957).
- [20] F. GINELLI, P. POGGI, A. TURCHI, H. CHATÉ, R. LIVI, AND A. POLITI, *Characterizing dynamics with covariant Lyapunov vectors*, Phys. Rev. Lett., 99 (2007), paper 130601. [arXiv:0706.0510](https://arxiv.org/abs/0706.0510).
- [21] M. GOLUBITSKY AND I. STEWART, *The Symmetry Perspective*, Birkhäuser Boston, Cambridge, MA, 2002.
- [22] J. M. GREENE AND J. S. KIM, *The steady states of the Kuramoto–Sivashinsky equation*, Phys. D, 33 (1988), pp. 99–120.
- [23] J. HAMILTON, J. KIM, AND F. WALEFFE, *Regeneration mechanisms of near-wall turbulence structures*, J. Fluid Mech., 287 (1995), pp. 317–348.
- [24] B. HOF, C. W. H. VAN DOORNE, J. WESTERWEEL, F. T. M. NIEUWSTADT, H. FAISST, B. ECKHARDT, H. WEDIN, R. R. KERSWELL, AND F. WALEFFE, *Experimental observation of nonlinear traveling waves in turbulent pipe flow*, Science, 305 (2004), pp. 1594–1598.
- [25] P. HOLMES, J. L. LUMLEY, AND G. BERKOOZ, *Turbulence, Coherent Structures, Dynamical Systems and Symmetry*, Cambridge University Press, Cambridge, UK, 1996.
- [26] E. HOPF, *A mathematical example displaying features of turbulence*, Comm. Appl. Math., 1 (1948), pp. 303–322.

- [27] J. M. HYMAN, B. NICOLAENKO, AND S. ZALESKI, *Order and complexity in the Kuramoto–Sivashinsky model of weakly turbulent interfaces*, Phys. D, 23 (1986), pp. 265–292.
- [28] M. E. JOHNSON, M. S. JOLLY, AND I. G. KEVREKIDIS, *The Oseberg transition: Visualization of global bifurcations for the Kuramoto–Sivashinsky equation*, Internat. J. Bifur. Chaos Appl. Sci. Engrg., 11 (2001), pp. 1–18.
- [29] M. JOLLY, R. ROSA, AND R. TEMAM, *Evaluating the dimension of an inertial manifold for the Kuramoto–Sivashinsky equation*, Adv. Differential Equations, 5 (2000), pp. 31–66.
- [30] A.-K. KASSAM AND L. N. TREFETHEN, *Fourth-order time-stepping for stiff PDEs*, SIAM J. Sci. Comput., 26 (2005), pp. 1214–1233.
- [31] G. KAWAHARA AND S. KIDA, *Periodic motion embedded in plane Couette turbulence: Regeneration cycle and burst*, J. Fluid Mech., 449 (2001), pp. 291–300.
- [32] I. G. KEVREKIDIS, B. NICOLAENKO, AND J. C. SCOVEL, *Back in the saddle again: A computer assisted study of the Kuramoto–Sivashinsky equation*, SIAM J. Appl. Math., 50 (1990), pp. 760–790.
- [33] B. KRAUSKOPF, H. OSINGA, E. DOEDEL, M. HENDERSON, J. GUCKENHEIMER, A. VLADIMIRSKY, M. DELLNITZ, AND O. JUNGE, *A survey of methods for computing (un)stable manifolds of vector fields*, Internat. J. Bifur. Chaos Appl. Sci. Engrg., 15 (2005), pp. 763–791.
- [34] M. KRUPA, *Bifurcations of relative equilibria*, SIAM J. Math. Anal., 21 (1990), pp. 1453–1486.
- [35] M. KRUPA, *Robust heteroclinic cycles*, J. Nonlinear Sci., 7 (1997), p. 129.
- [36] Y. KURAMOTO AND T. TSUZUKI, *Persistent propagation of concentration waves in dissipative media far from thermal equilibrium*, Progr. Theoret. Phys., 55 (1976), p. 365.
- [37] Y. LAN, *Dynamical Systems Approach to One-Dimensional Spatiotemporal Chaos—A Cyclist’s View*, Ph.D. thesis, School of Physics, Georgia Institute of Technology, Atlanta, GA, 2004; available online at <http://etd.gatech.edu/theses/available/etd-10282004-154606/>.
- [38] Y. LAN AND P. CVITANOVIĆ, *Unstable recurrent patterns in Kuramoto–Sivashinsky dynamics*, Phys. Rev. E, 78 (2008), paper 026208. [arXiv.org:0804.2474](https://arxiv.org/abs/0804.2474).
- [39] R. E. LAQUEY, S. M. MAHAJAN, P. H. RUTHERFORD, AND W. M. TANG, *Nonlinear saturation of the trapped-ion mode*, Phys. Rev. Lett., 34 (1974), pp. 391–394.
- [40] V. LÓPEZ, P. BOYLAND, M. T. HEATH, AND R. D. MOSER, *Relative periodic solutions of the complex Ginzburg–Landau equation*, SIAM J. Appl. Dyn. Syst., 4 (2005), pp. 1042–1075.
- [41] P. MANNEVILLE, *Dissipative Structures and Weak Turbulence*, Academic Press, Boston, 1990.
- [42] D. MICHELSON, *Steady solutions of the Kuramoto–Sivashinsky equation*, Phys. D, 19 (1986), pp. 89–111.
- [43] J. J. MORÉ, B. S. GARBOW, AND K. E. HILLSTROM, *User Guide for MINPACK-1*, report ANL-80-74, Argonne National Laboratory, Argonne, IL, 1980.
- [44] E. SIMINOS, *Recurrent Spatio-Temporal Structures in Presence of Continuous Symmetries*, Ph.D. thesis, School of Physics, Georgia Institute of Technology, Atlanta, GA, 2009; available online at <http://ChaosBook.org/projects/Siminos/thesis.pdf>.
- [45] E. SIMINOS, P. CVITANOVIĆ, AND R. L. DAVIDCHACK, *Recurrent spatio-temporal structures of translationally invariant Kuramoto–Sivashinsky flow*, manuscript, 2009.
- [46] G. I. SIVASHINSKY, *Nonlinear analysis of hydrodynamical instability in laminar flames—I. Derivation of basic equations*, Acta Astronaut., 4 (1977), p. 1177.
- [47] V. SZEBEHELY, *Theory of Orbits*, Academic Press, New York, 1967.
- [48] D. VISWANATH, *Recurrent motions within plane Couette turbulence*, J. Fluid Mech., 580 (2007), pp. 339–358. [arXiv:physics/0604062](https://arxiv.org/abs/physics/0604062).
- [49] H.-L. YANG, K. A. TAKEUCHI, F. GINELLI, H. CHATÉ, AND G. RADONS, *Hyperbolicity and the effective dimension of spatially-extended dissipative systems*, Phys. Rev. Lett., 102 (2009), paper 074102. [arXiv:0807.5073](https://arxiv.org/abs/0807.5073).